Supplementary materials

Si-doped nitrogenated holey graphene (C₂N) as a promising gas sensor for O-containing volatile organic compounds (VOCs) and ammonia
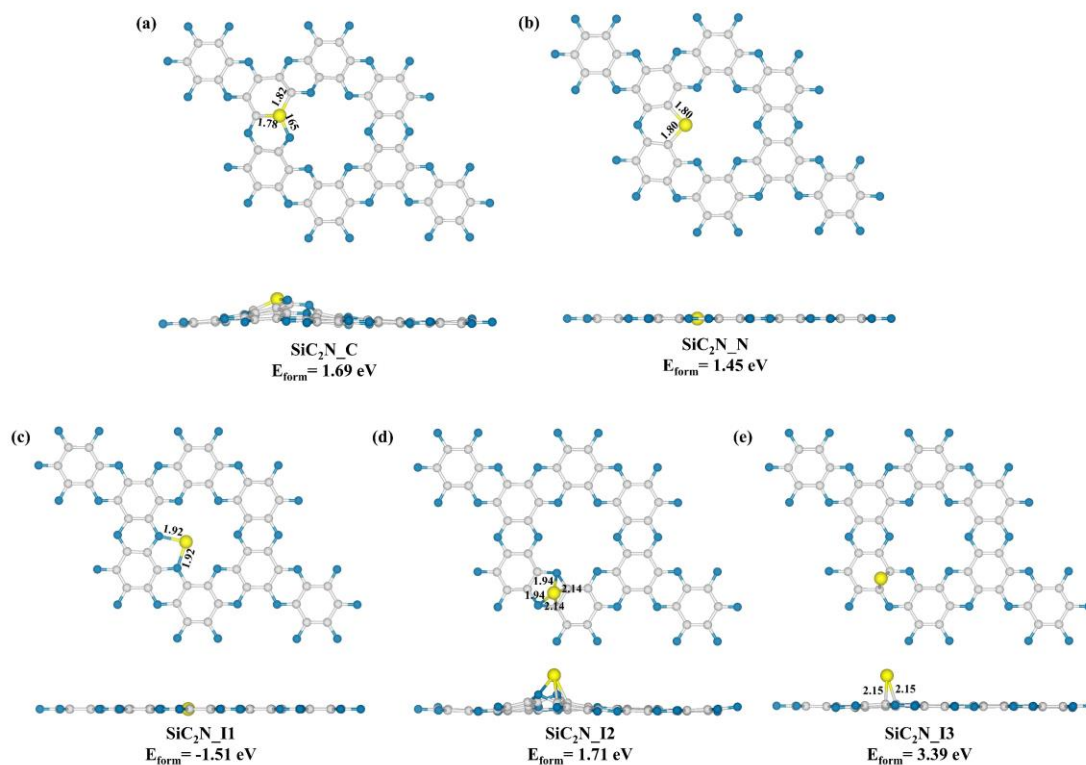

Figure S1. Optimized structures of (**a**) SiC₂N_C, (**b**) SiC₂N_N, (**c**) SiC₂N_I1, and (**d**) SiC₂N_I2, and (**e**) SiC₂N_I3 systems, the corresponding formation energies are given. (Grey: C atom, Blue: N atom, Yellow: Si atom)
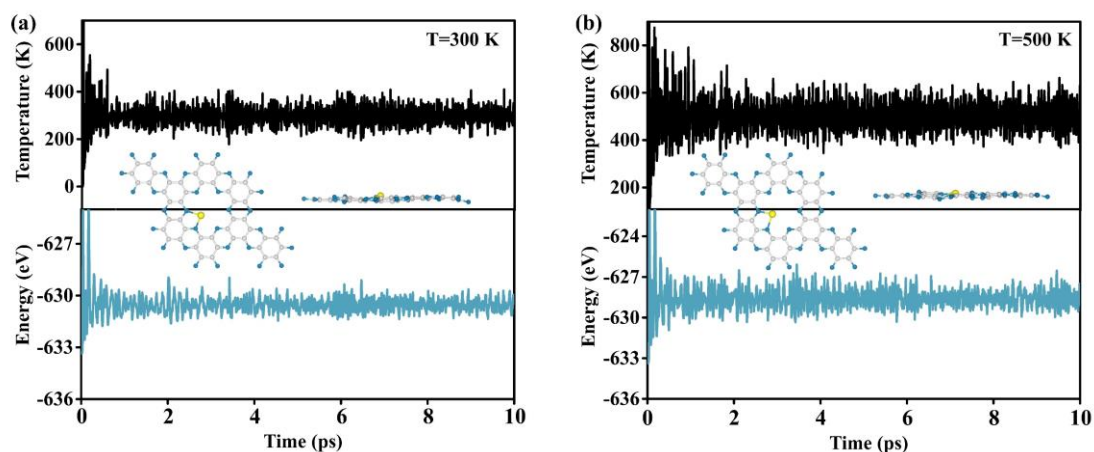

Figure S2. Variations of temperatures and energies against the time for AIMD simulations of SiC₂N at (**a**) 300 and (**b**) 500 K, insets are top and side views of the snapshots of atomic configuration at 10 ps.
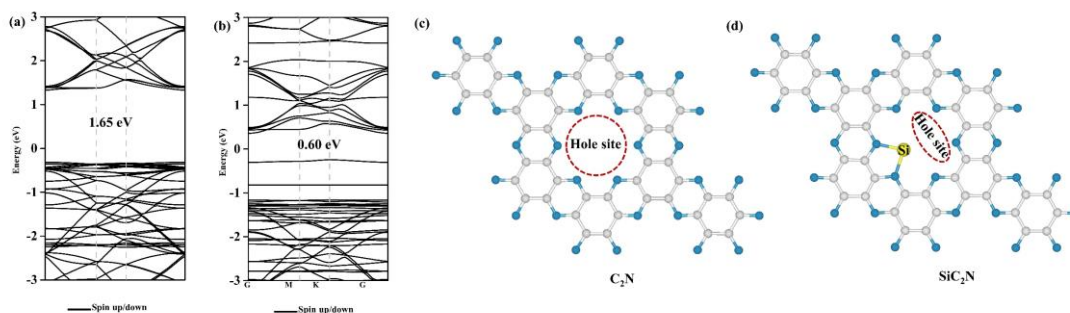
Figure S3. The band strucures of (**a**) C₂N and (**b**) SiC₂N with PBE method; the adsorption sites of (**c**) C₂N and (**d**) SiC₂N for VOCs and ammonia. (Grey: C atom, Blue: N atom, Yellow: Si atom)
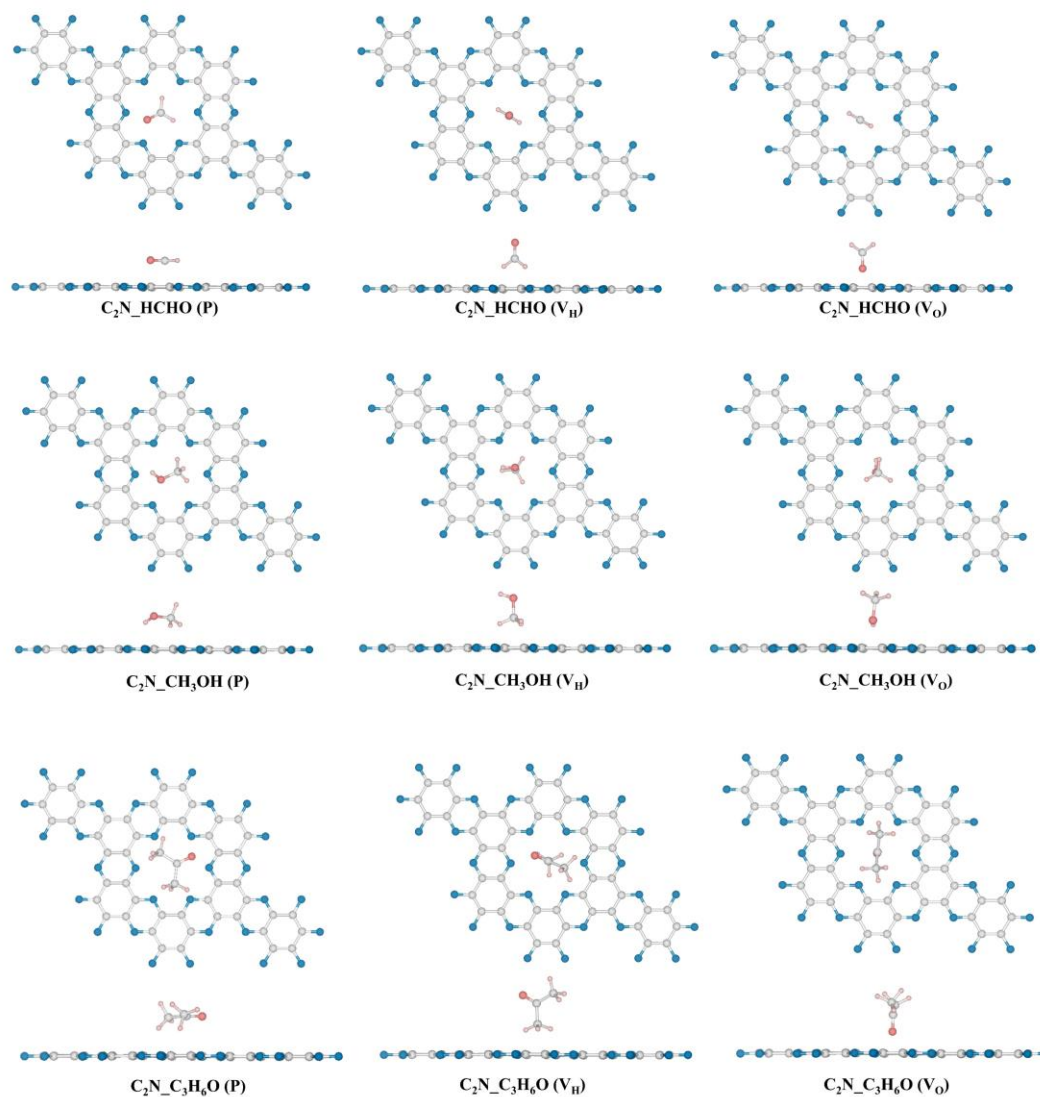

Figure S4. The initial adsorption configurations of HCHO, CH₃OH, and C₃H₆O molecules on the hole site of pristine C₂N. Note that the adsorption patterns of gases on C₂N are labeled in brackets, in which the "P" and "V" represent the gases placed on C₂N in parallel and vertical positions, respectively. In addition, the subscript of the "V" are the interaction sites of gas molecules. (Grey: C atom, Blue: N atom, Red: O atom, Pink: H atom)
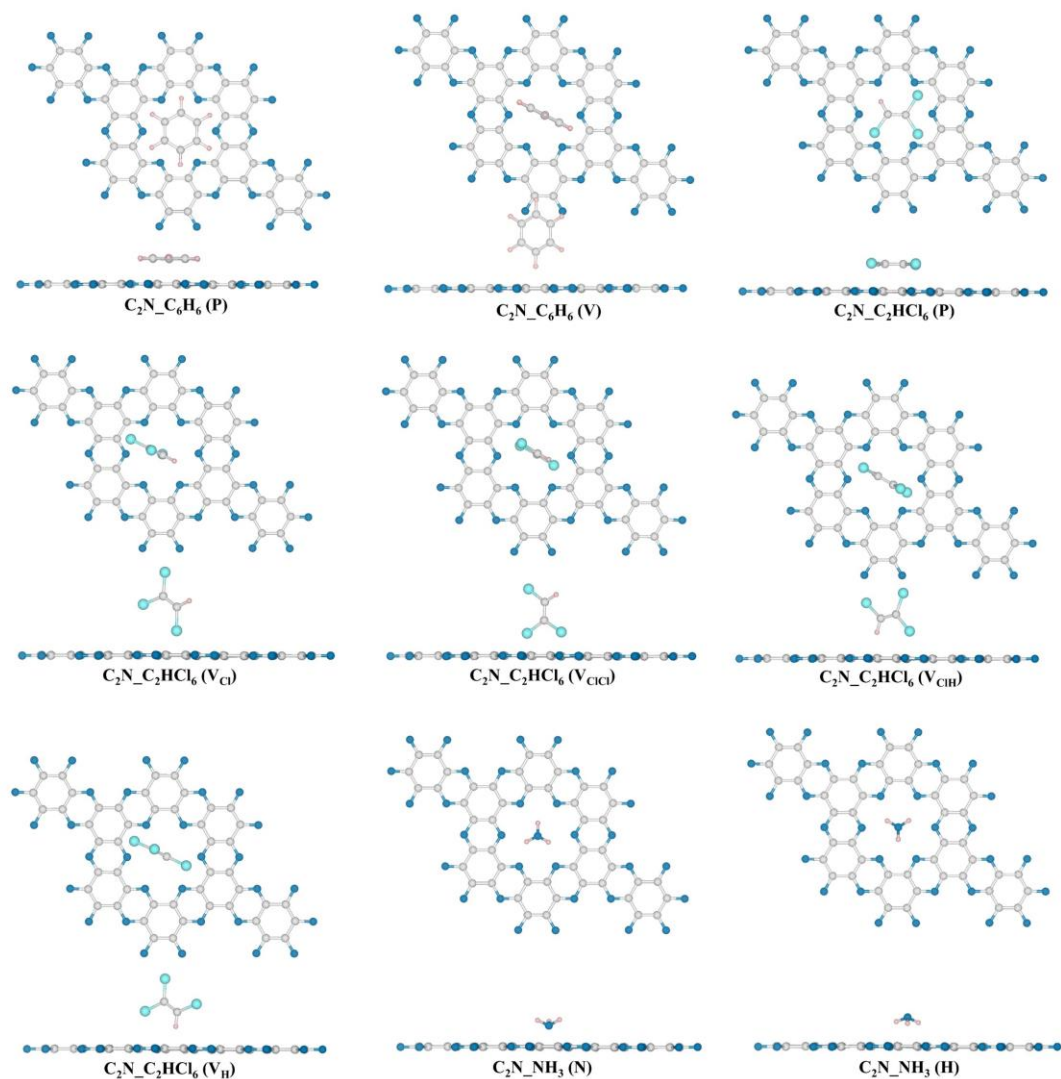
Figure S5. The initial adsorption configurations of C_6H_6, C_2HCl_3, and NH_3 molecules on the hole site of pristine C_2N. Note that the adsorption patterns of gases on C_2N are labeled in brackets, in which the "P" and "V" represent the gases placed on C_2N in parallel and vertical positions, respectively. In addition, the subscript of the "V" are the interaction sites of gas molecules. In particular, the "(N)" or "(H)" in the $C_2N\_NH_3$ systems donate the interaction sites of NH_3. (Grey: C atom, Blue: N atom, Cyan: Cl atom, Pink: H atom)
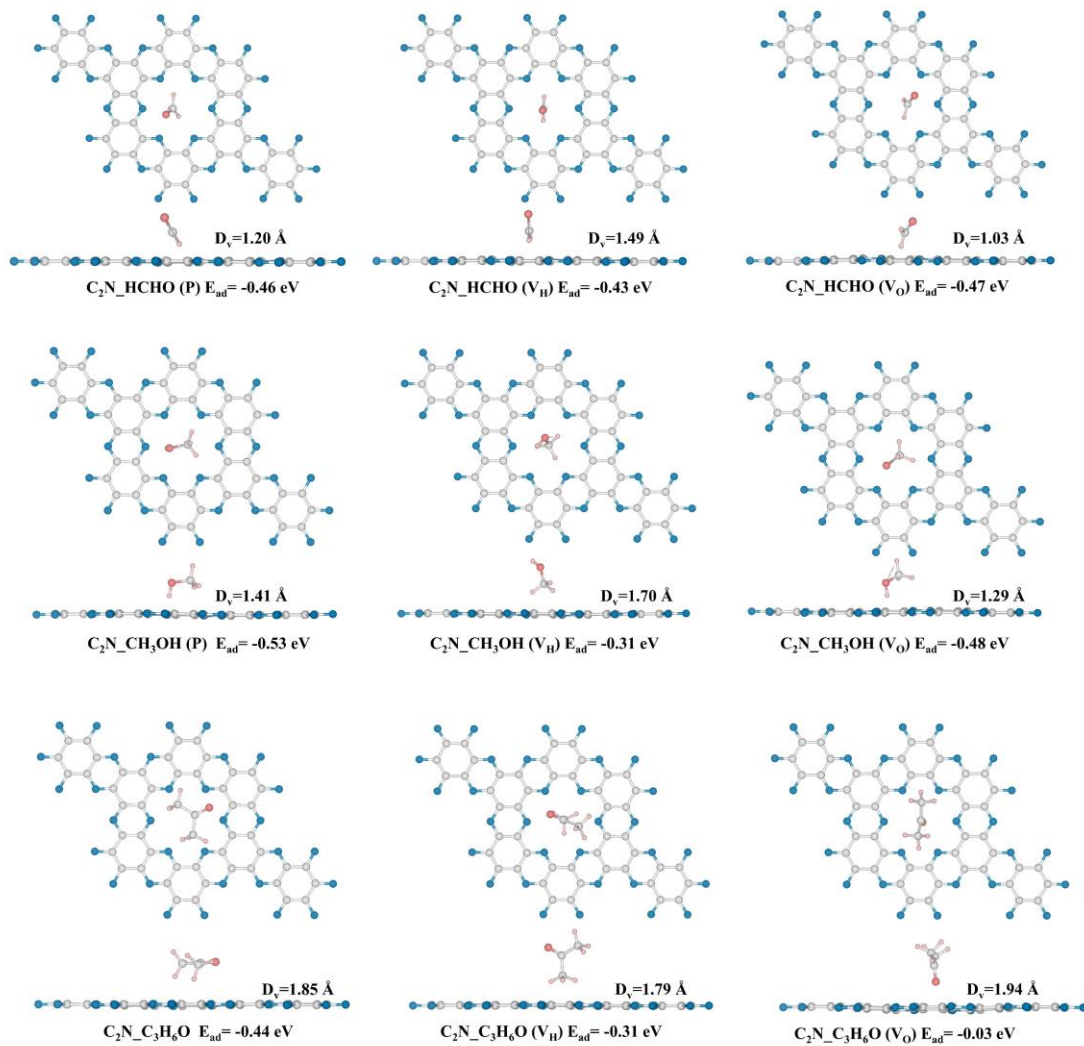
Figure S6. The optimized adsorption configurations of HCHO, CH₃OH, and C₃H₆O molecules on the hole site of pristine C₂N based on the initial configurations in Figure S4. (Grey: C atom, Blue: N atom, Red: O atom, Pink: H atom)
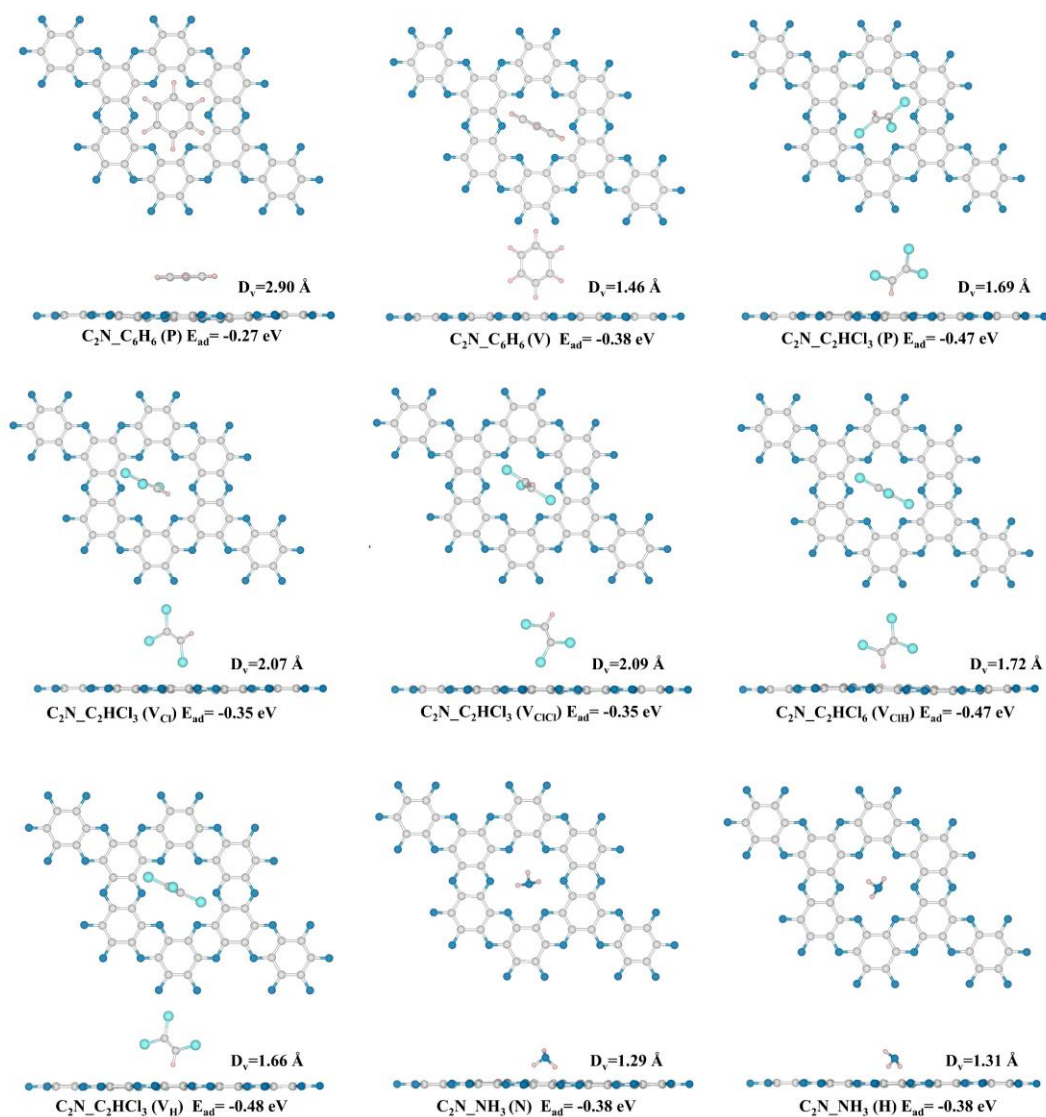
Figure S7. The optimized adsorption configurations of C_6H_6, C_2HCl_3, and NH_3 molecules on the hole site of pristine C_2N based on the initial configurations in Figure S5. (Grey: C atom, Blue: N atom, Cyan: Cl atom, Pink: H atom)
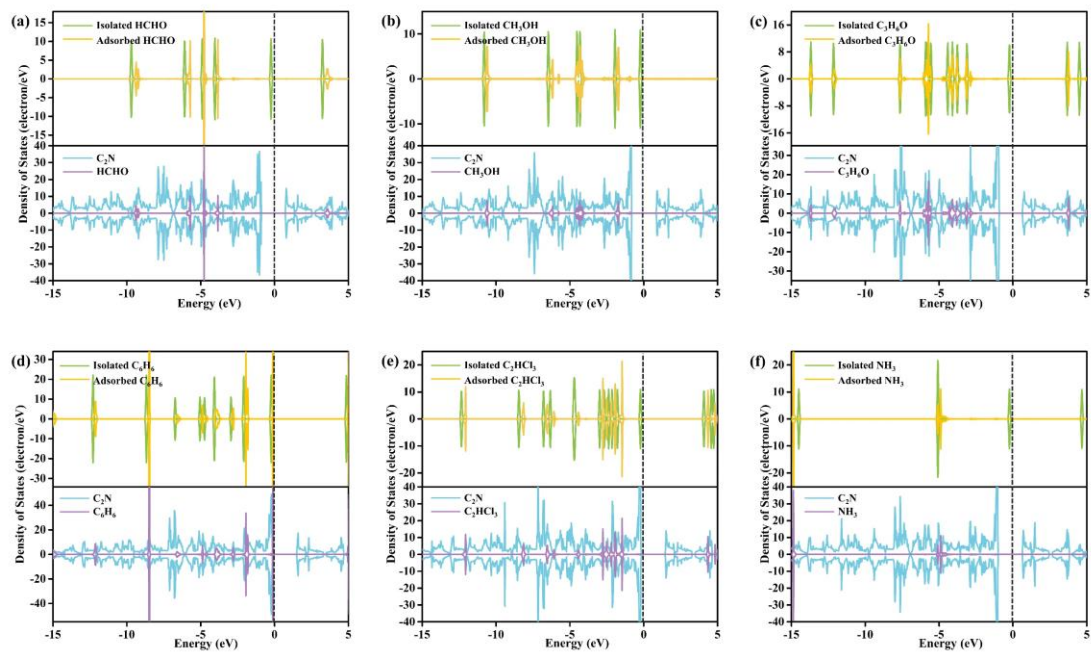
**Figure S8**. The density of states of gases before and after adsorption, the partial density of states of C_2N and gases for (**a**) C_2N_HCHO, (**b**) $C_2N\_CH_3OH$, (**c**) $C_2N\_C_3H_6O$, (**d**) $C_2N\_C_6H_6$, (**e**) $C_2N\_C_2HCl_3$ and (**f**) $C_2N\_NH_3$ systems.
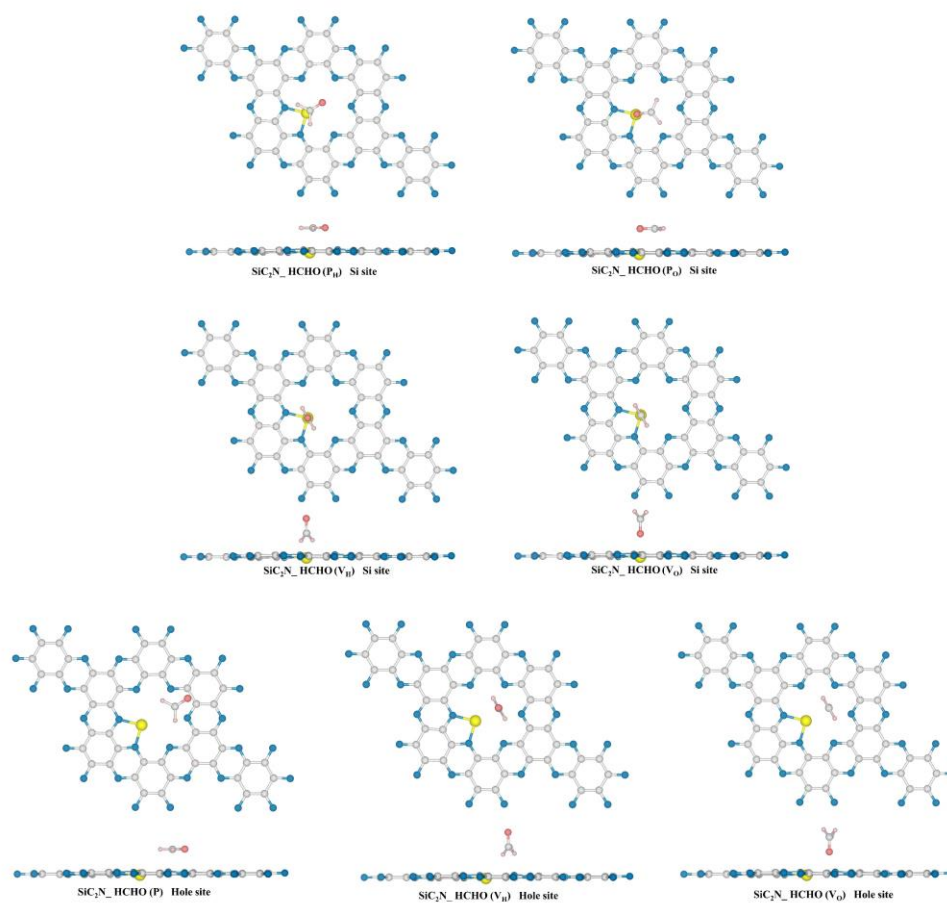
Figure S9. The initial adsorption configurations of HCHO molecule on the Si and hole site of SiC$_2$N. Note that the adsorption patterns of gases on SiC$_2$N were labeled in brackets, in which the "P" and "V" represented the HCHO placed on SiC$_2$N surface in parallel and vertical positions, respectively. In addition, the subscript of the "P" or "V" are the interaction sites of HCHO. (Grey: C atom, Blue: N atom, Red: O atom, Yellow: Si atom, Pink: H atom)
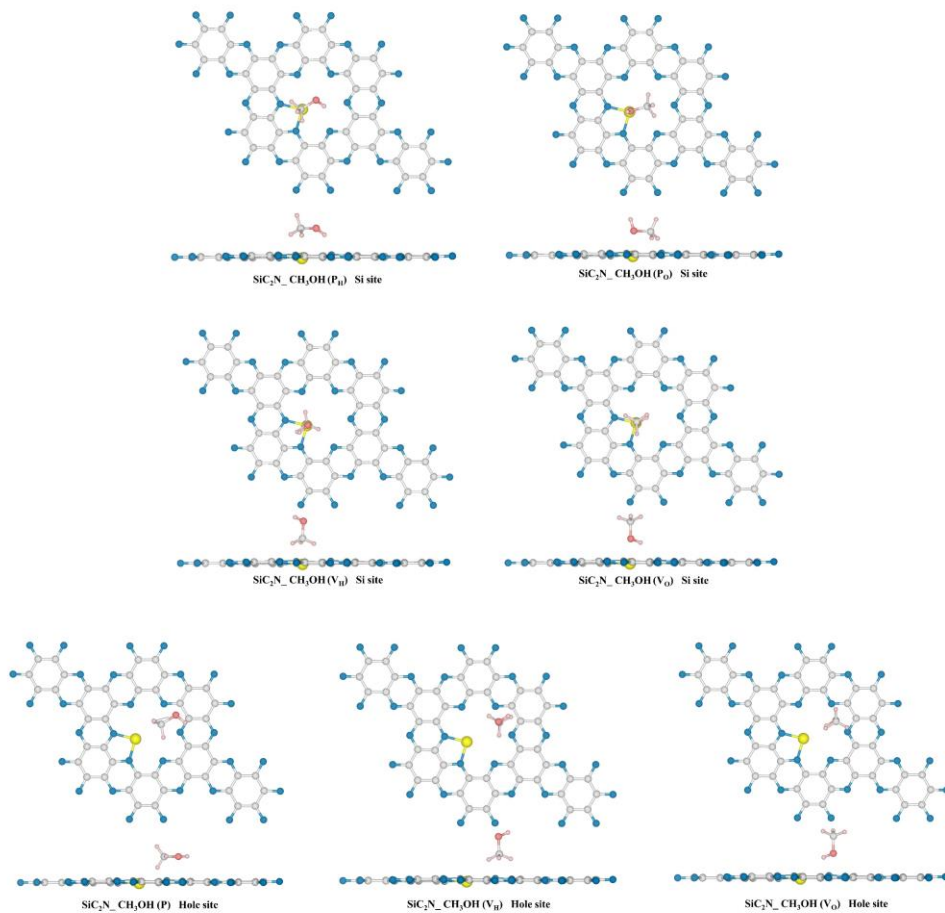
Figure S10. The initial adsorption configurations of CH₃OH molecule on the Si and hole site of SiC2N. Note that the adsorption patterns of gases on SiC2N were labeled in brackets, in which the "P" and "V" represented the CH₃OH placed on SiC2N surface in parallel and vertical positions, respectively. In addition, the subscript of the "P" or "V" are the interaction sites of CH₃OH. (Grey: C atom, Blue: N atom, Red: O atom, Yellow: Si atom, Pink: H atom)
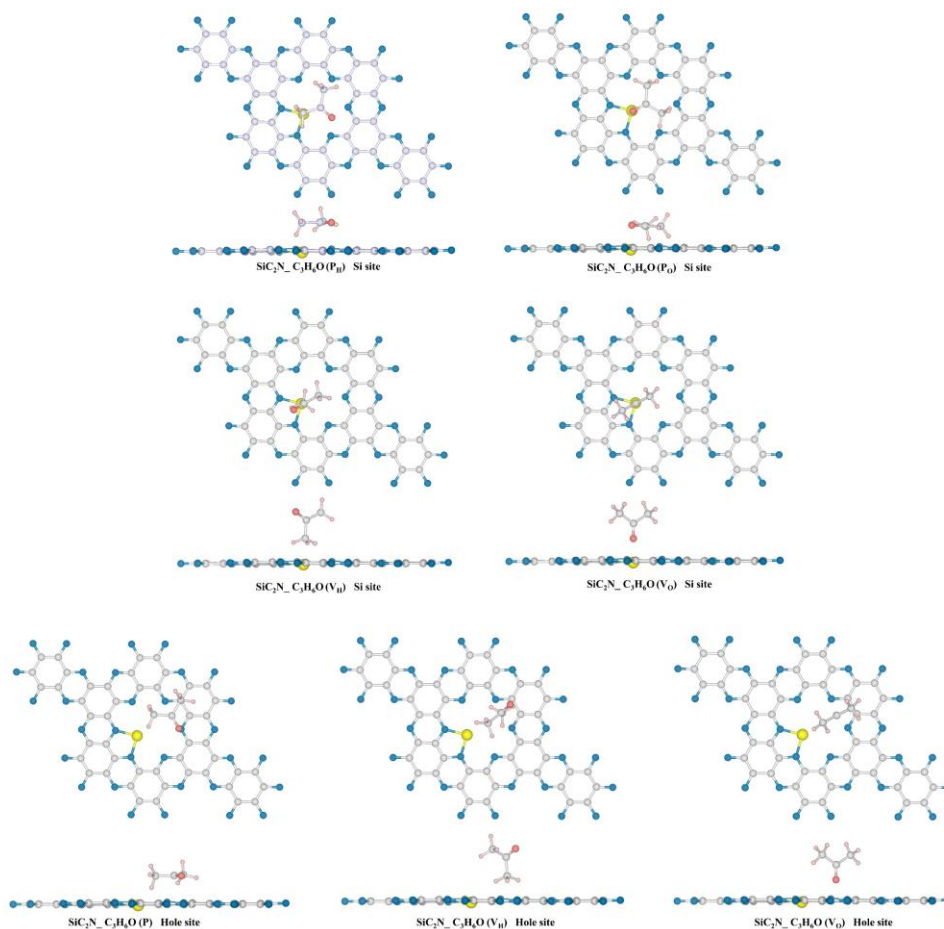
Figure S11. The initial adsorption configurations of C_3H_6O molecule on the Si and hole site of SiC$_2$N. Note that the adsorption patterns of gases on SiC$_2$N were labeled in brackets, in which the "P" and "V" represented the C_3H_6O placed on SiC$_2$N surface in parallel and vertical positions, respectively. In addition, the subscript of the "P" or "V" are the interaction sites of C_3H_6O. (Grey: C atom, Blue: N atom, Red: O atom, Yellow: Si atom, Pink: H atom)
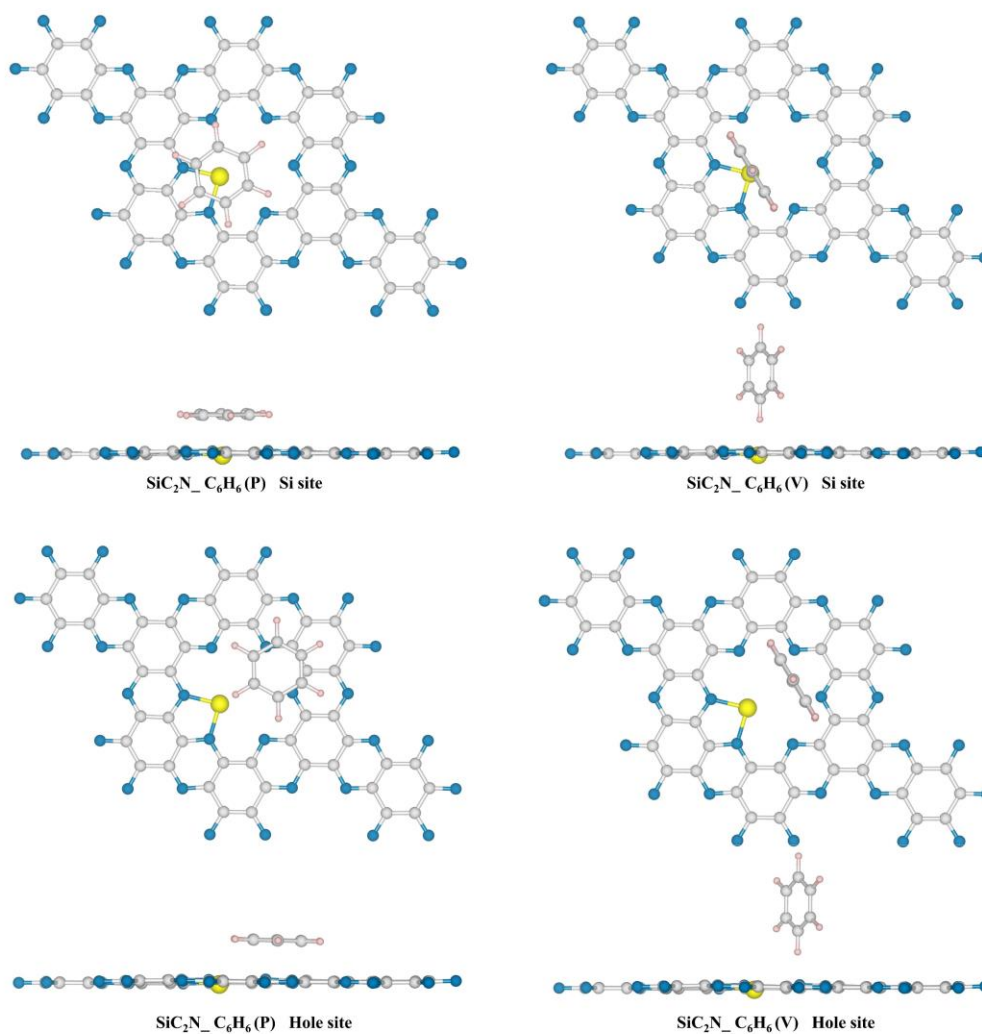
Figure S12. The initial adsorption configurations of C_6H_6 molecule on the Si and hole site of SiC_2N. Note that the adsorption patterns of gases on SiC_2N were labeled in brackets, in which the "P" and "V" represented the C_6H_6 placed on SiC_2N surface in parallel and vertical positions, respectively. (Grey: C atom, Blue: N atom, Yellow: Si atom, Pink: H atom)
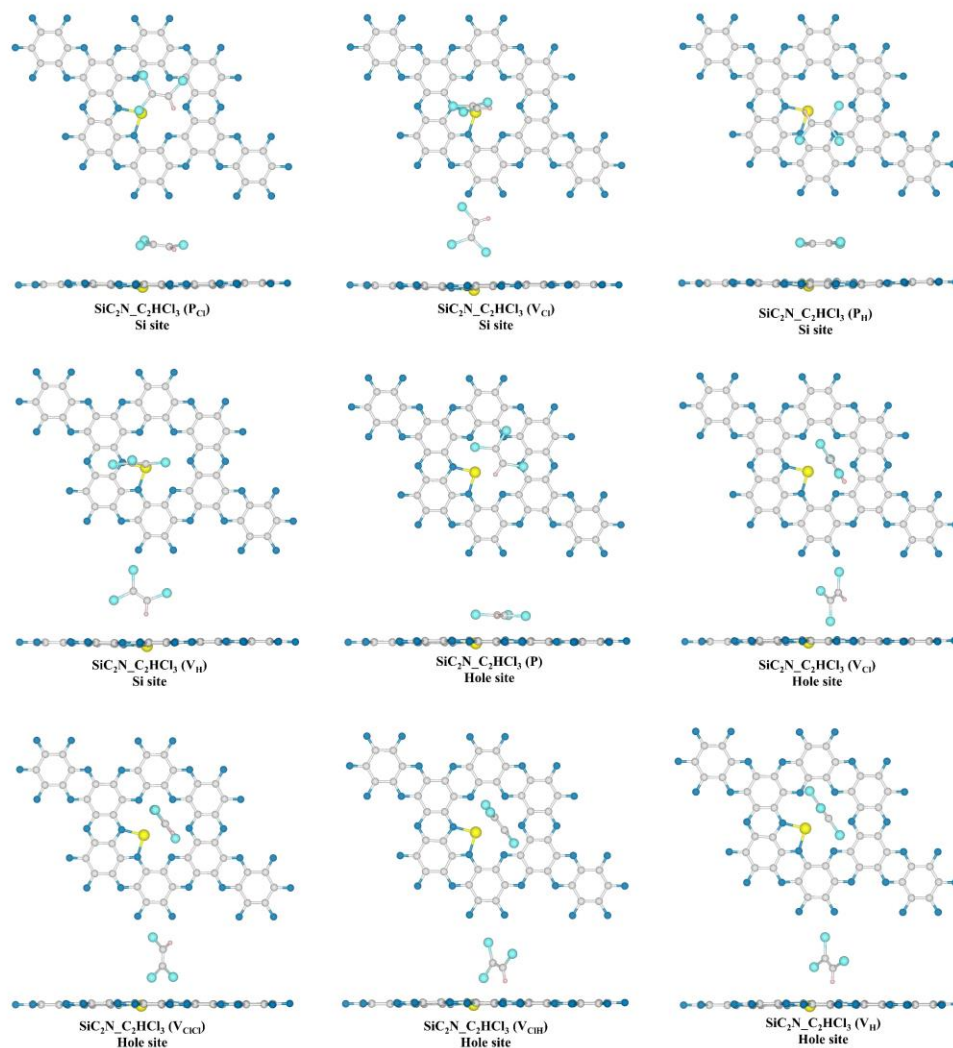
Figure S13. The initial adsorption configurations of C_2HCl_3 molecule on the Si and hole site of SiC_2N. Note that the adsorption patterns of gases on SiC_2N were labeled in brackets, in which the "P" and "V" represented the C_2HCl_3 placed on SiC_2N surface in parallel and vertical positions, respectively. In addition, the subscript of the "P" or "V" are the interaction sites of C_2HCl_3 molecule. (Grey: C atom, Blue: N atom, Cyan: Cl atom, Yellow: Si atom, Pink: H atom)
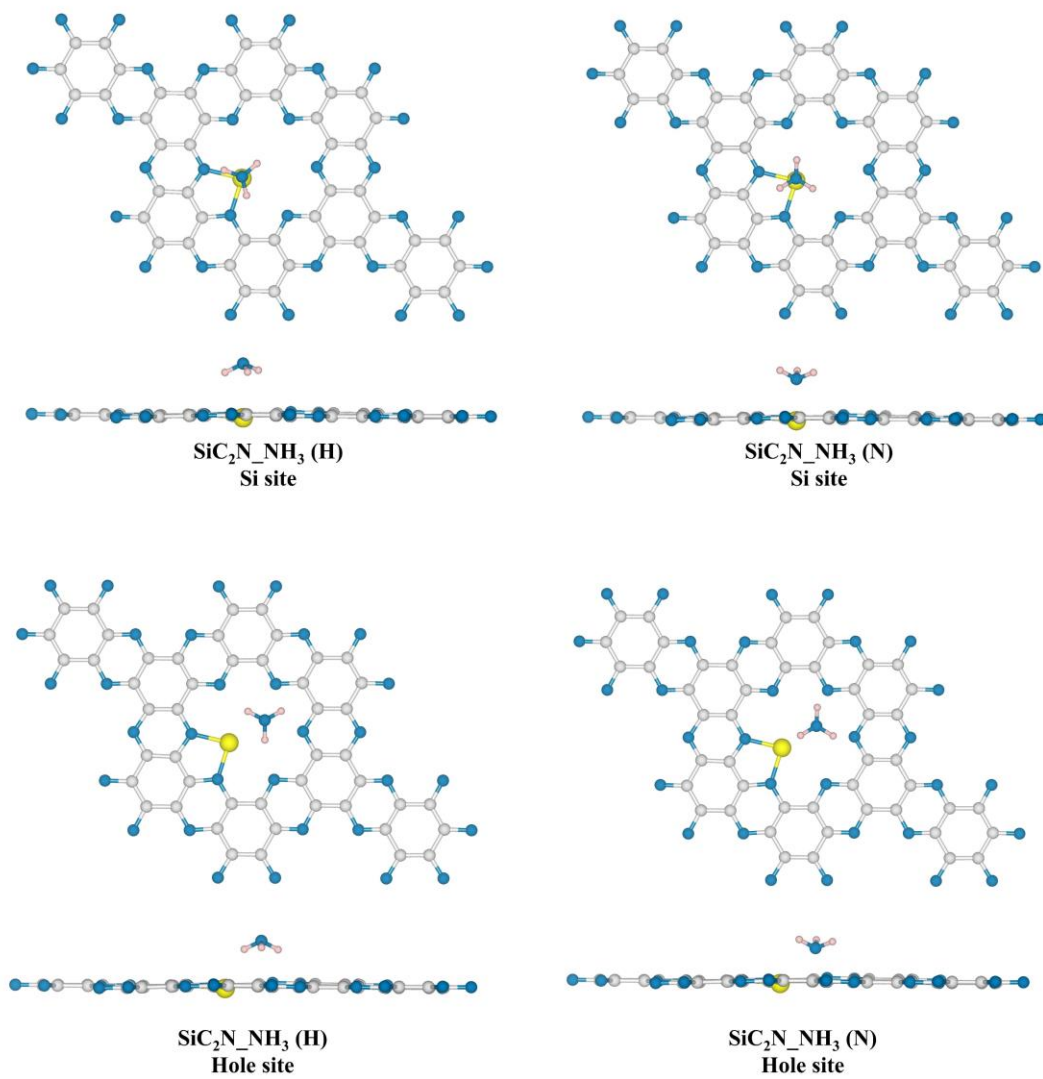
Figure S14. The initial adsorption configurations of NH$_3$ molecule on the Si and hole site of SiC$_2$N. The adsorption sites of NH$_3$ (N or H) were labeled in brackets. (Grey: C atom, Blue: N atom, Yellow: Si atom, Pink: H atom)
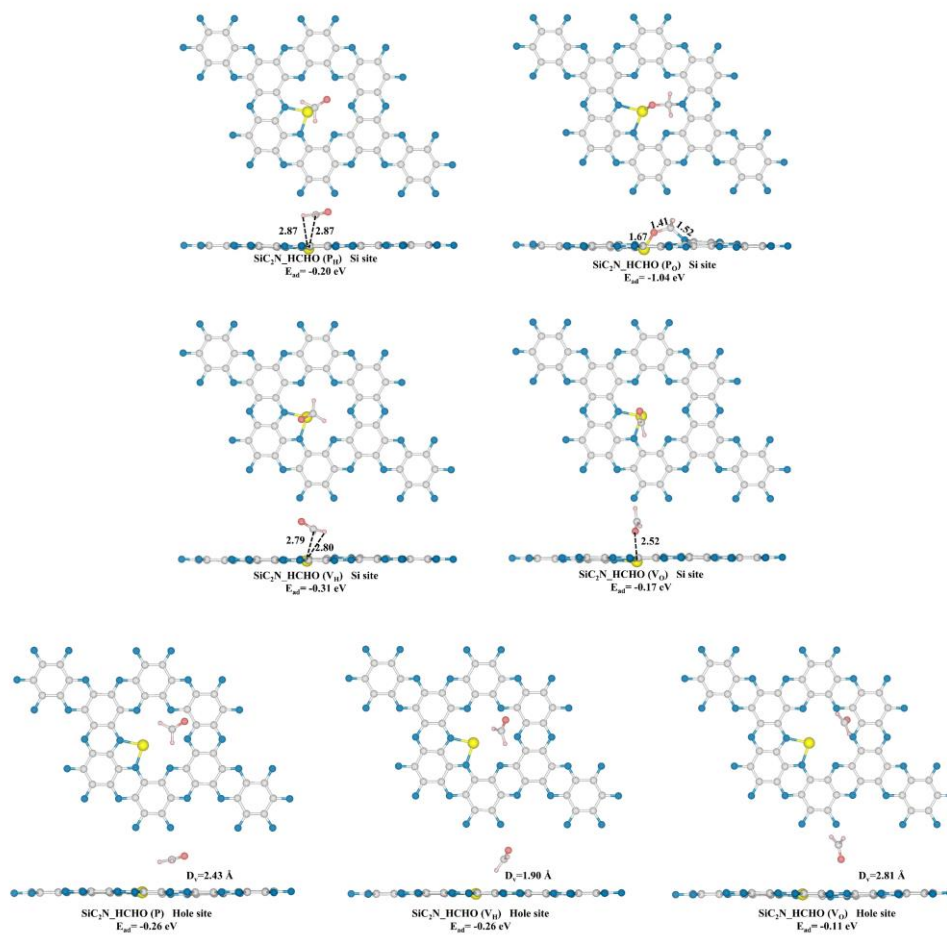
Figure S15. The optimized adsorption configurations of SiC$_2$N_HCHO systems based on the initial configurations in Figure S9. (Grey: C atom, Blue: N atom, Red: O atom, Yellow: Si atom, Pink: H atom)
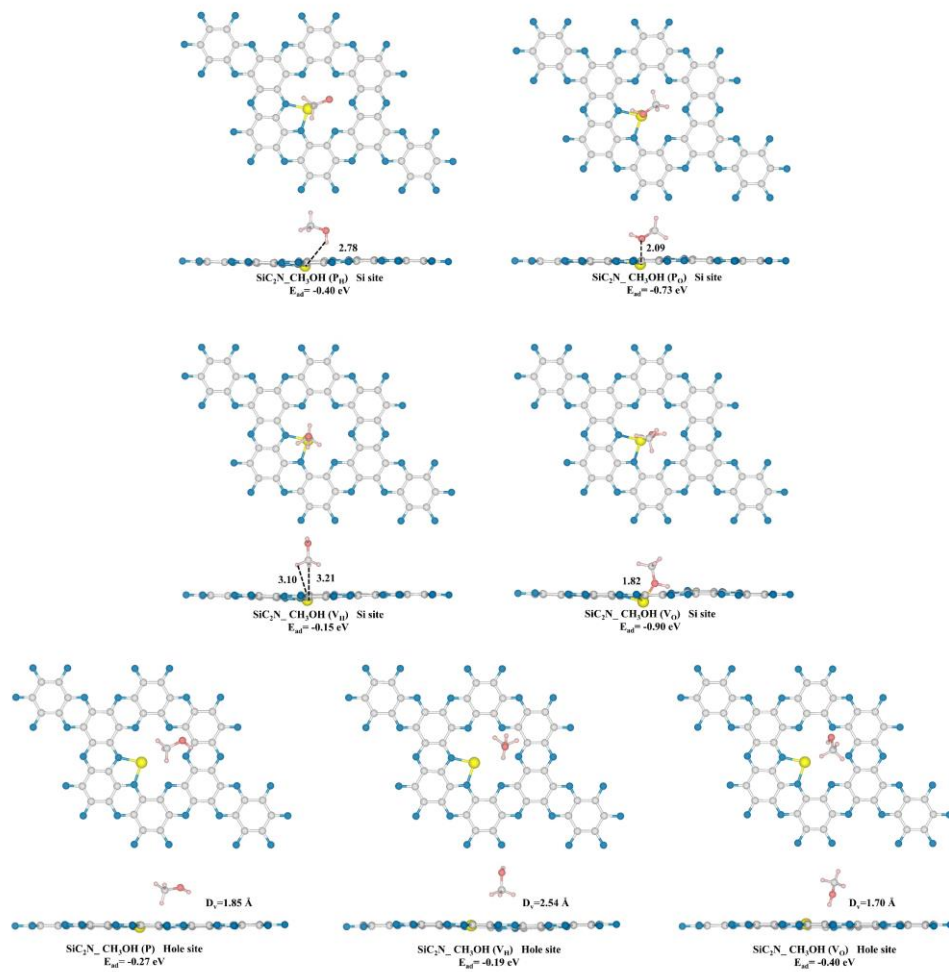
Figure S16. The optimized adsorption configurations of SiC₂N_CH₃OH systems based on the initial configurations in Figure S10. (Grey: C atom, Blue: N atom, Yellow: Si atom, Red: O atom, Pink: H atom)
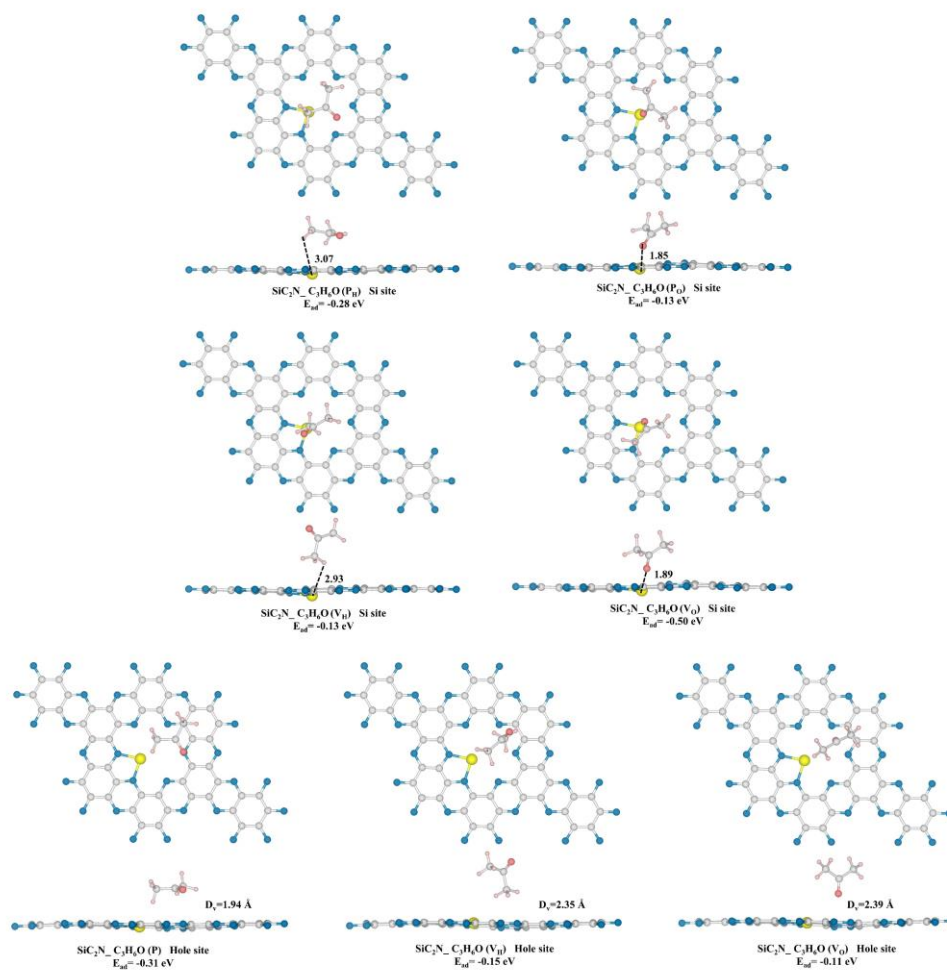
Figure S17. The optimized adsorption configurations of SiC$_2$N_C$_3$H$_6$O systems based on the initial configurations in Figure S11. (Grey: C atom, Blue: N atom, Yellow: Si atom, Red: O atom, Pink: H atom)
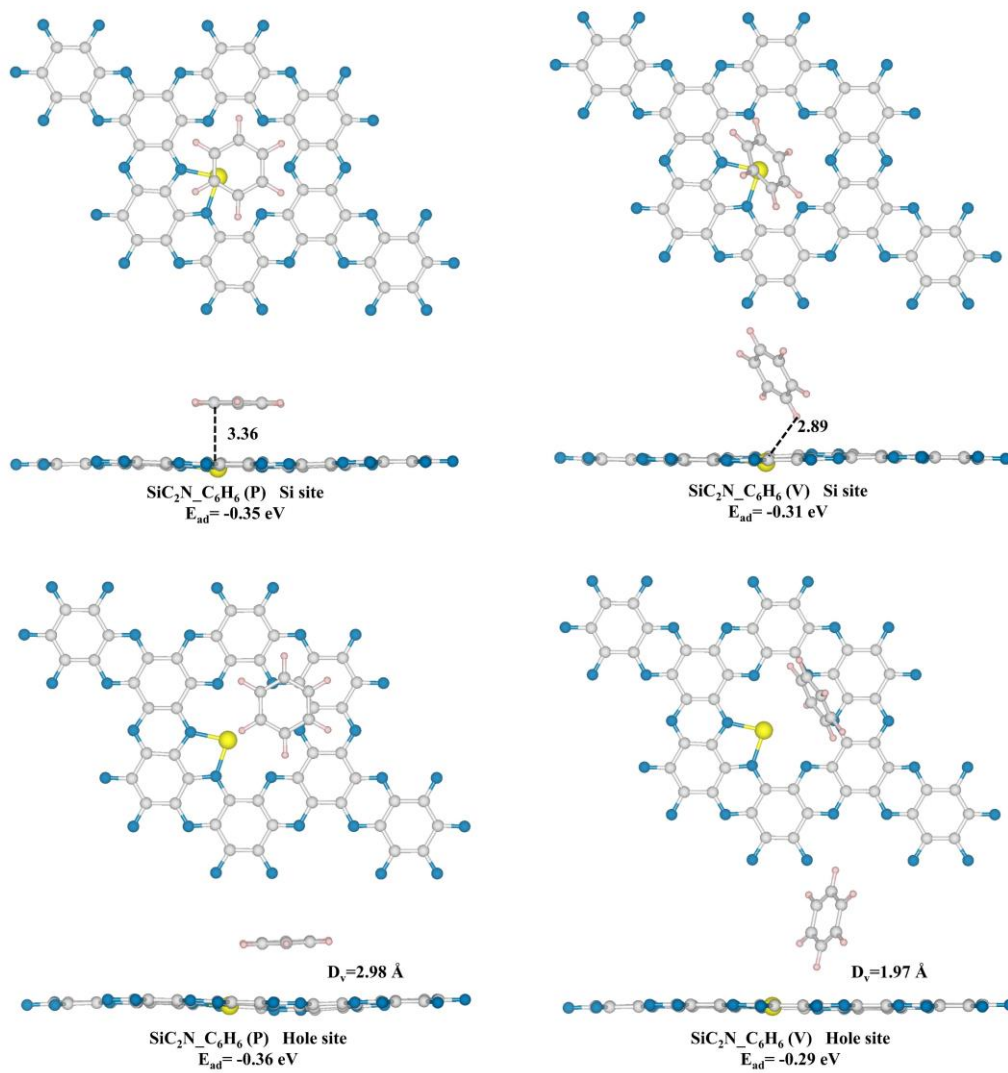
Figure S18. The optimized adsorption configurations of SiC$_2$N_C$_6$H$_6$ systems based on the initial configurations in Figure S12. (Grey: C atom, Blue: N atom, Yellow: Si atom, Pink: H atom)
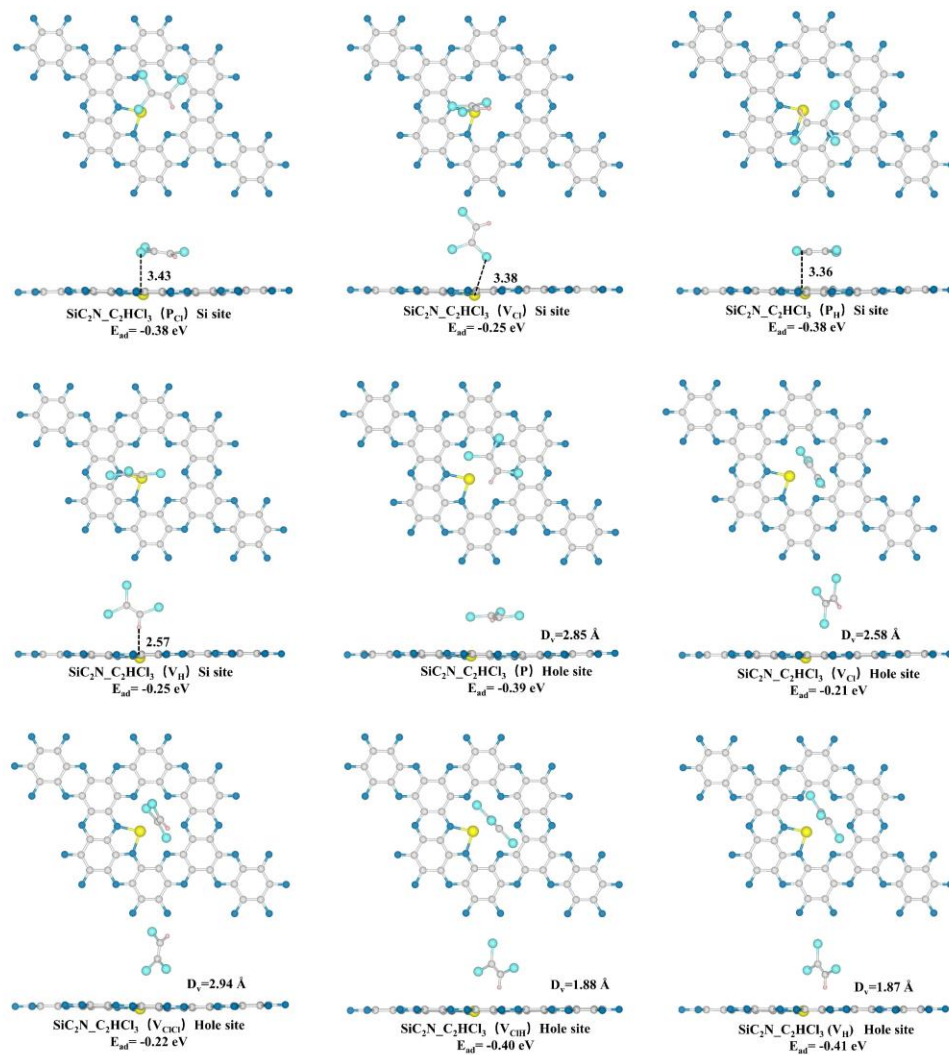
Figure S19. The optimized adsorption configurations of SiC$_2$N_C$_6$H$_6$ systems based on the initial configurations in Figure S13. (Grey: C atom, Blue: N atom, Yellow: Si atom, Cyan: Cl atom, Pink: H atom)
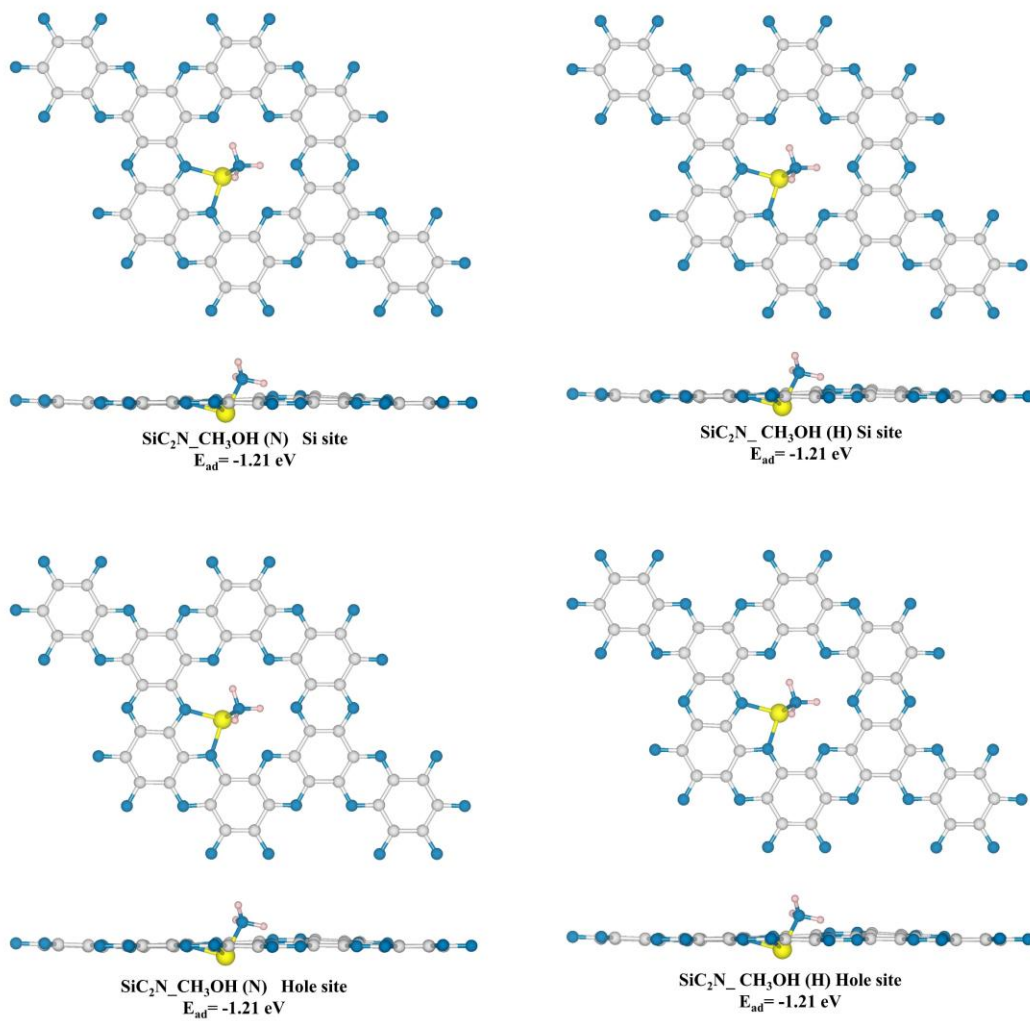
Figure S20. The optimized adsorption configurations of SiC$_2$N_NH$_3$ systems based on the initial configurations in Figure S14. (Grey: C atom, Blue: N atom, Yellow: Si atom, Pink: H atom)
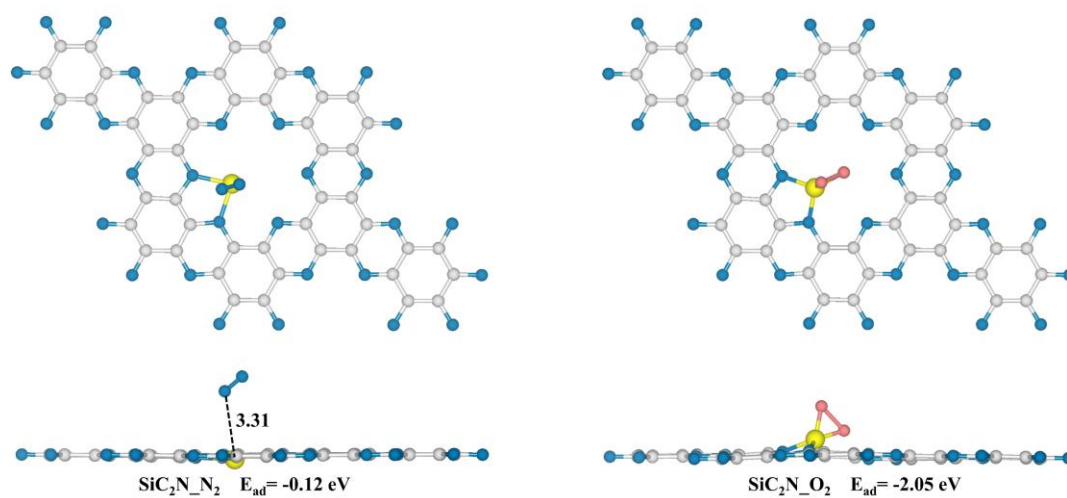

Figure S21. The optimal binding configurations of N$_2$ and O$_2$ on SiC$_2$N. Bonds are in Å. (Silvery: C atom, Blue: N atom, Yellow: Si atom, Red: O atom)
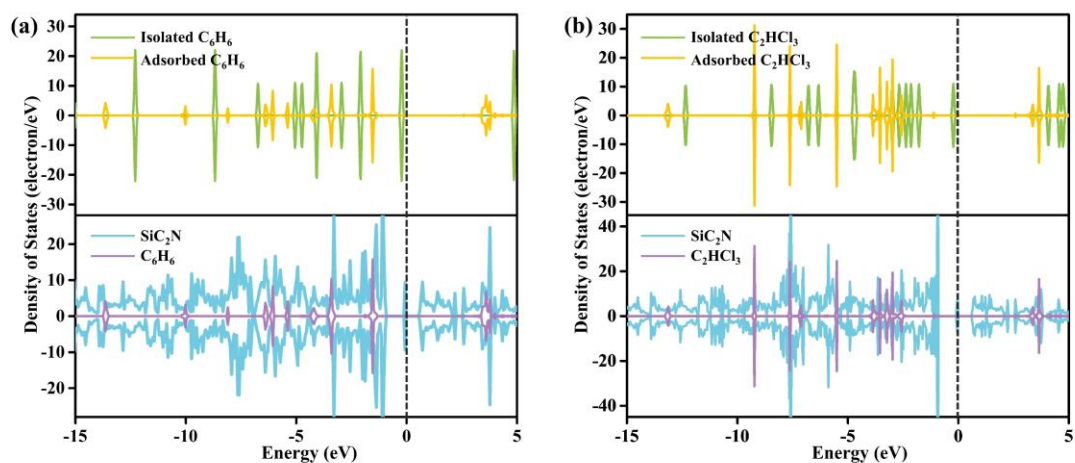
Figure S22. The density of states of gases before and after adsorption, the partial density of states of SiC$_2$N and gases for (**a**) SiC$_2$N_C$_6$H$_6$ and (**b**) SiC$_2$N_C$_2$HCl$_3$ systems.
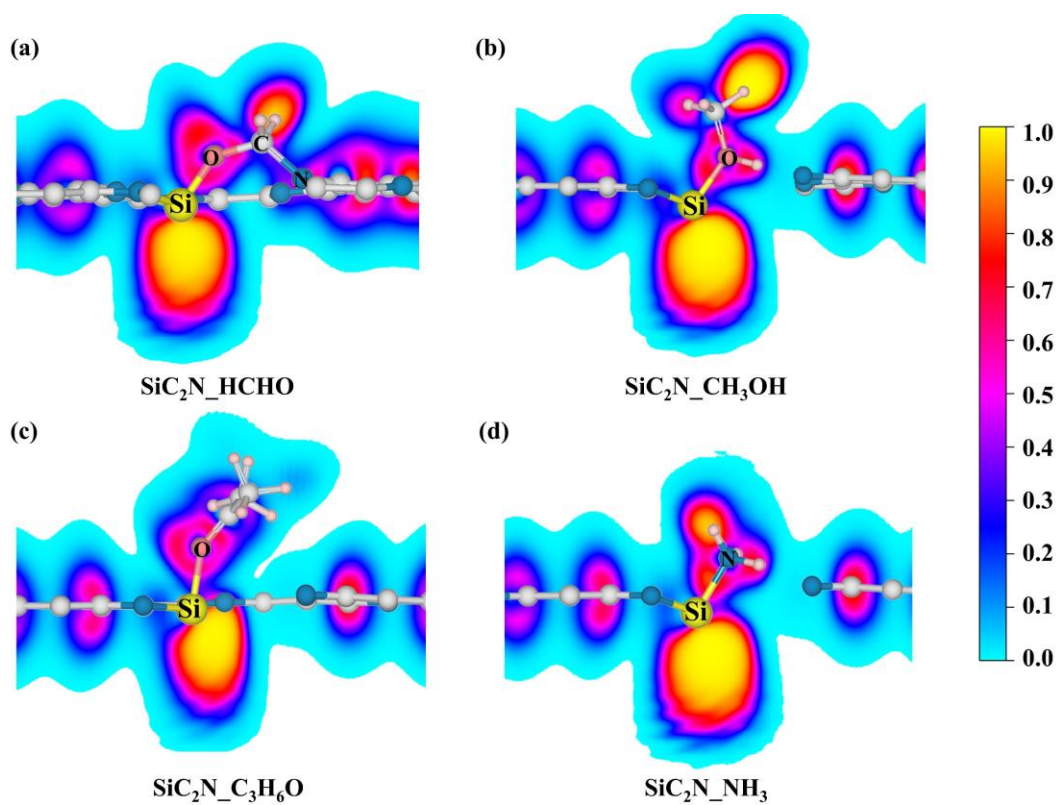
Figure S23. The electron localization function (ELF) diagrams of (**a**) SiC$_2$N_HCHO, (**b**) SiC$_2$N_CH$_3$OH, (**c**) SiC$_2$N_C$_3$H$_6$O, and (**d**) SiC$_2$N_NH$_3$ systems, in which partial atoms are hidden for better reading.
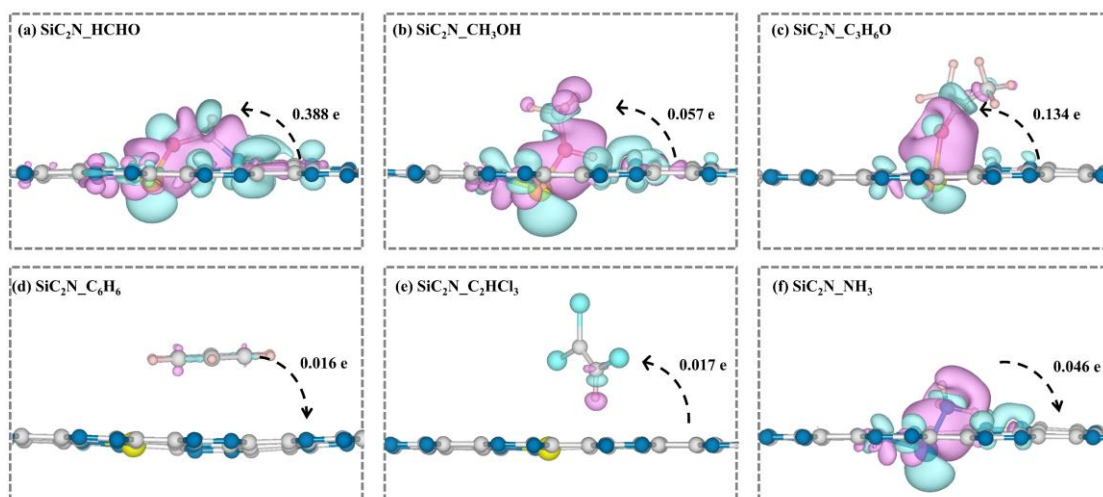
Figure S24. The charge density difference between gases and SiC₂N in (**a**) SiC₂N_HCHO, (**b**) SiC₂N_CH₃OH, (**c**) SiC₂N_C₃H₆O, (**d**) SiC₂N_C₆H₆, (**e**) SiC₂N_C₂HCl₃, and (**f**) SiC₂N_NH₃ systems. The cyan and magenta bubbles donate the charge accumulation and depletion, respectively, with the isodensity value set as 0.002 e/Bohr³. (Grey: C atom, Blue: N atom, Yellow: Si atom, Cyan: Cl atom, Red: O atom, Pink: H atom)
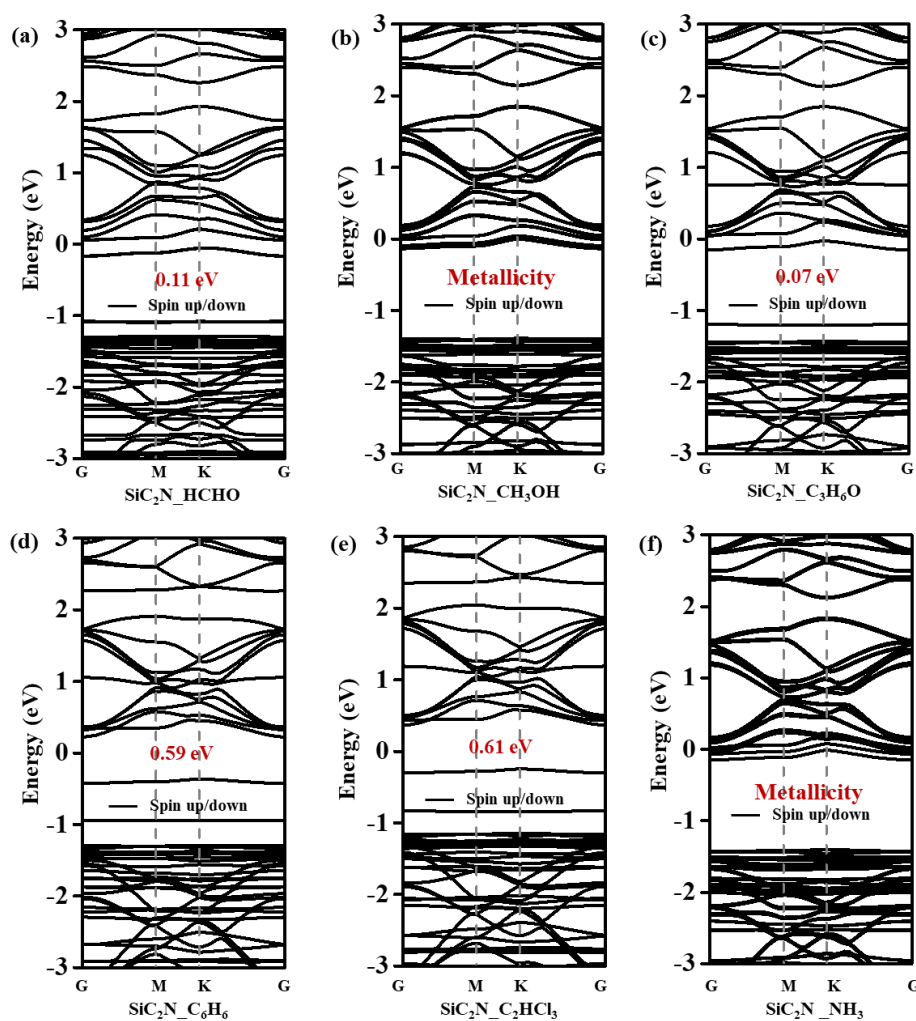
Figure S25. Band structures of (**a**) SiC₂N_HCHO, (**b**) SiC₂N_CH₃OH, (**c**) SiC₂N_C₃H₆O, (**d**) SiC₂N_C₆H₆, (**e**) SiC₂N_C₂HCl₃, and (**f**) SiC₂N_NH₃ systems within PBE method.
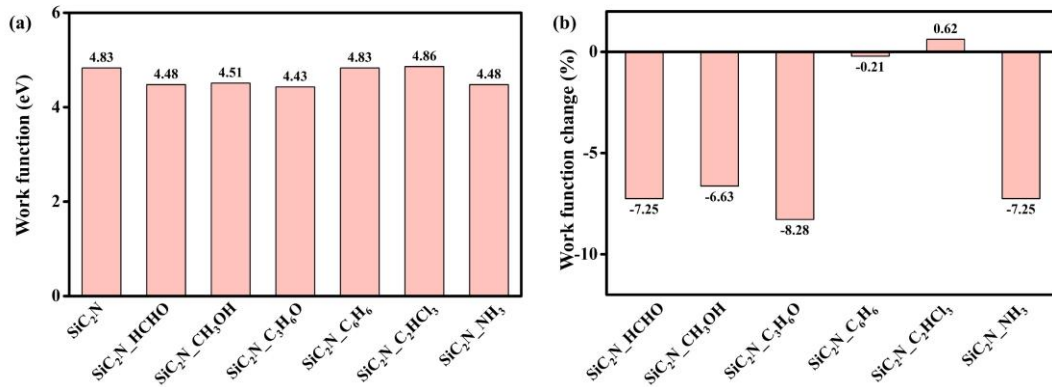
Figure S26. (**a**) The work function and (**b**) work function changes of SiC$_2$N and SiC$_2$N_gas systems.

Herein, we also evaluated the performance of SiC$_2$N as a Φ-type sensor, the Φ changes of the systems will interrupt the gate voltage and thus are reflected in electrical signals [1,2]. Therefore, it is necessary to estimate the work function changes caused by gas adsorption. The work function is defined as the minimum energy required for one electron escaping from the Fermi level:

$$\Phi = E_{vac} - E_F \tag{1}$$

where the E_{vac} and E_F donate the energy of vacuum energy level and Fermi energy level, respectively. And the obtained Φ values for SiC$_2$N_gas systems as well as the changes were presented in Figure S25(a) and (b), respectively. It can be observed that the adsorption of O-containing VOCs and ammonia leads to work function drops of SiC$_2$N. However, the relatively small Φ changes (-6.63%~-8.28%) may cause the SiC$_2$N to suffer from low sensitivity in the realistic application.
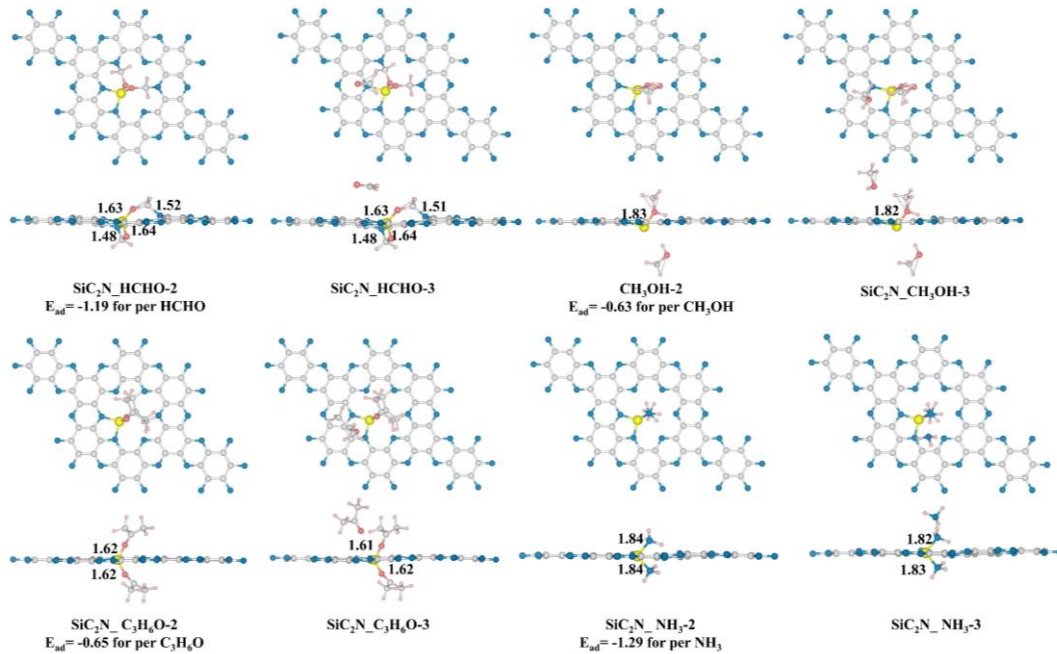
Figure S27. The adsorption configurations of two or three same gases on the SiC$_2$N sheet. Bonds are in Å.
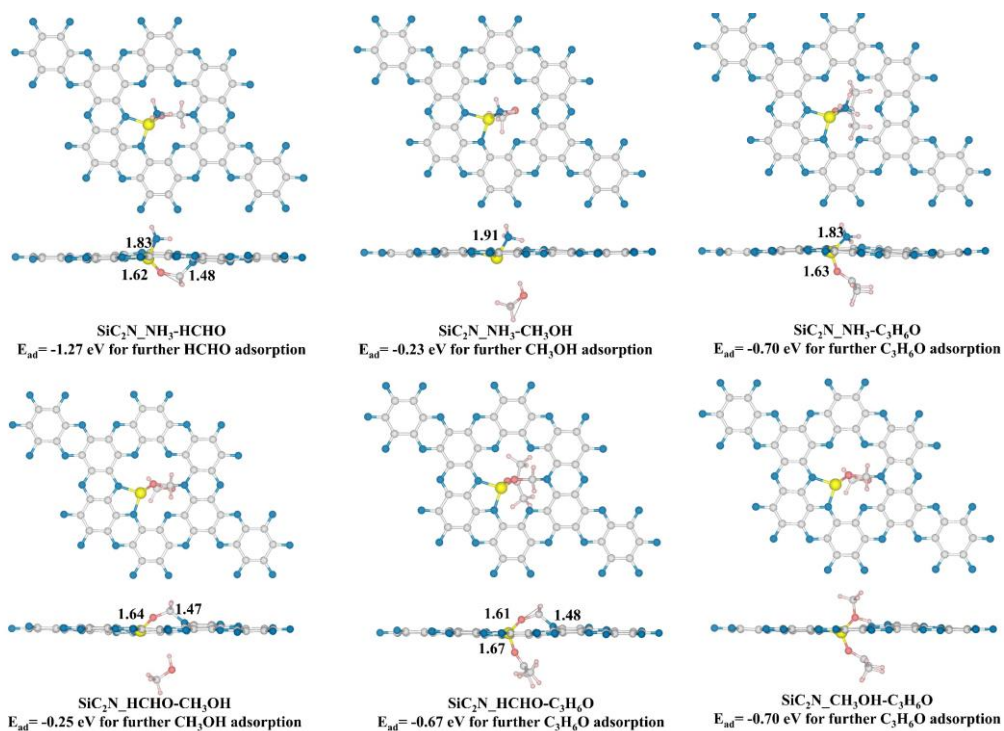
Figure S28. The adsorption configurations of two kinds of gases on the SiC₂N sheet. Bonds are in Å.
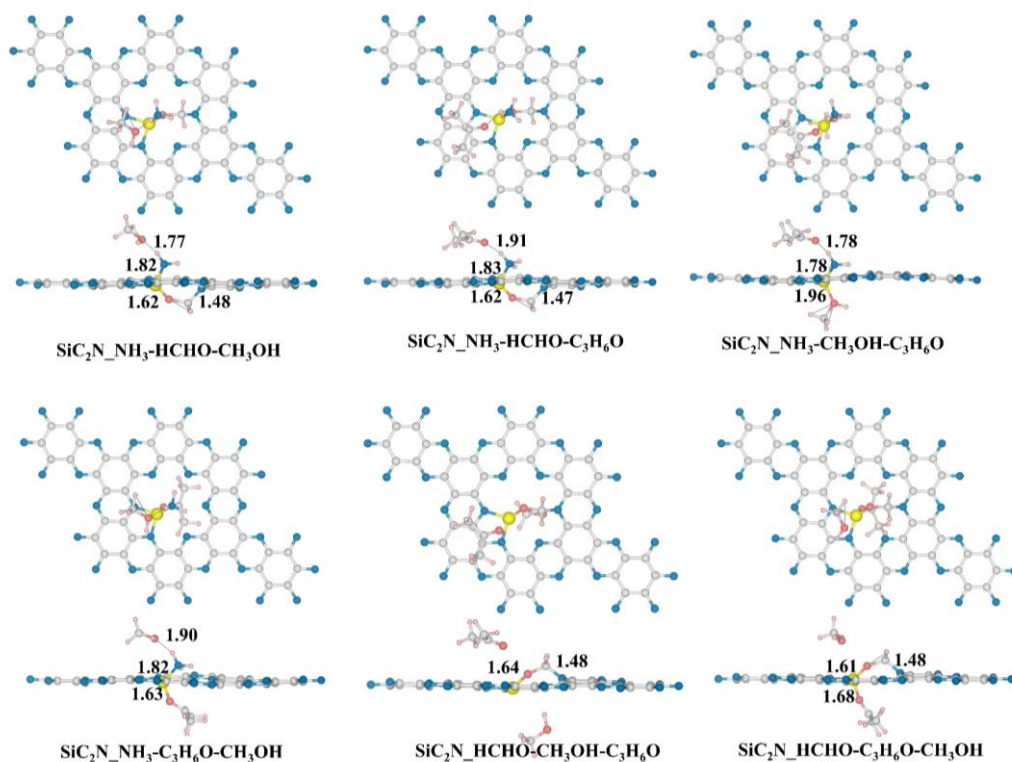
Figure S29. The adsorption configurations of three kinds of gases on the SiC₂N sheet. Bonds are in Å.
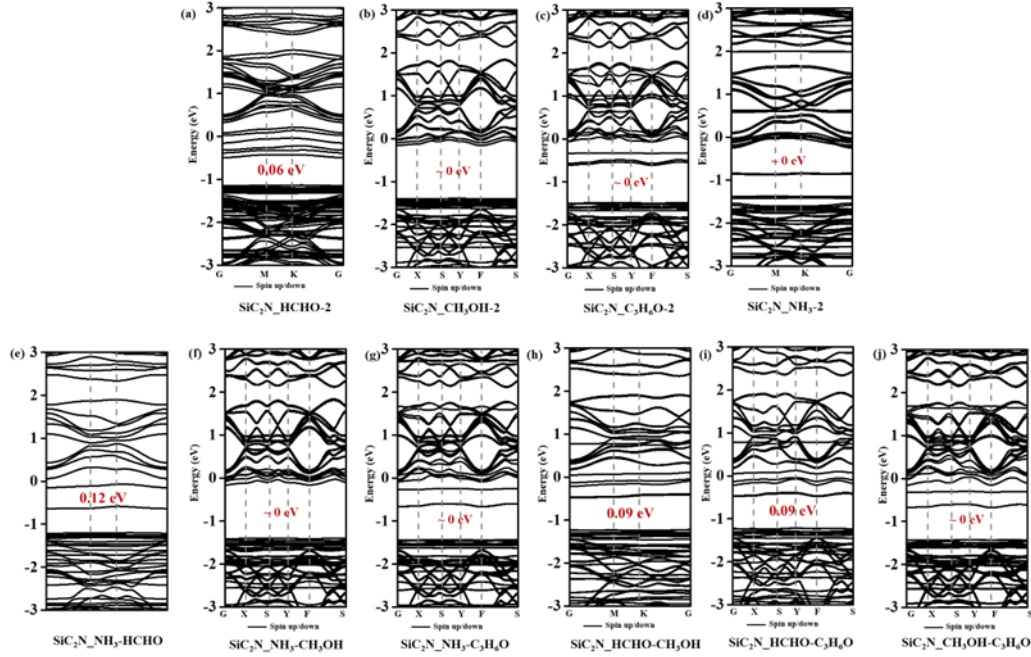
Figure S30. The band structures of the two-molecules adsorption system.

Herein, the effect of gas co-adsorption on the sensor performance of SiC$_2$N was investigated. Firstly, we evaluated the adsorption of a single kind of gas with high gas concentration, as displayed in Figure S27. It can be seen that, apart from the CH$_3$OH system, the SiC$_2$N can adsorb two gaseous molecules simultaneously. And the additional molecules physically adsorb on the SiC$_2$N sheet. For the two-molecules adsorbed systems, the adsorption energies per HCHO, C$_3$H$_6$O, and NH$_3$ are -1.19, -0.65, and -1.29 eV, respectively, which are slightly higher than the corresponding single gas adsorbed systems (-1.02 for HCHO, -0.60 for C$_3$H$_6$O and -1.24 eV for NH$_3$). The higher adsorption energies may be ascribed that the Si atom is more stable as a tetracoordinate state. The band structures of two-molecule adsorbed systems were all evaluated. Herein, to save computational resources, we used the PBE functional. It can be seen that the adsorption of two HCHO molecules triggers remarkable decreases in the band gap (0.54 eV), and SiC$_2$N_CH$_3$OH-2, SiC$_2$N_C$_3$H$_6$O-2 as well as SiC$_2$N_NH$_3$-2 present metallicity, demonstrating the enhancement of the conductivity. Such results also suggest that the gas concentration or to say the coverage has little effect on the sensitivity of SiC$_2$N. Besides, the recovery time of these two-molecule adsorbed systems under UV light was summarized in Table S2. Although the recovery time is slightly longer than the corresponding single-molecule systems, it can be seen that by using UV light, all the gases can be effectively removed at 400 K.

Furthermore, we also probed the adsorption of different kinds of gases on the SiC$_2$N sheet in Figure S3. One can see that, similar to the situation of the same gas adsorption, the Si atom can adsorb two kinds of gases. Since the adsorption ability of pure SiC$_2$N towards O-containing VOCs and ammonia follows the order of NH$_3$>HCHO>CH$_3$OH>C$_3$H$_6$O. When different gases co-exist, the SiC$_2$N will preferentially adsorb the gases with higher adsorption energy. Therefore, we calculated the adsorption energies of HCHO, CH$_3$OH, and C$_3$H$_6$O on SiC$_2$N which has adsorbed one preferential gas. It can be seen that apart from partial systems containing CH$_3$OH, the adsorption of preferential gas can promote the adsorption of subsequent, leading to larger adsorption energy. For instance, after the SiC$_2$N adsorbed NH$_3$, the adsorption energy for SiC$_2$N_NH$_3$ to further adsorb HCHO is -1.27 eV, which is negative than the pure SiC$_2$N for HCHO (-1.02 eV). Through the comprehensive assessment of band structures (Figure S30) and recovery time (Table S2), the co-adsorption of different gases has little effect on the sensitivity, but slightly enlarges the recovery time. Nevertheless, the adsorbed gases can be successfully by exposing to UV light at 400 K. In all, the coverage and co-adsorption of different gases have little effect on the sensitivity but slightly increase the

recovery time. Therefore, in the real application, the environment with low gas concentration is more favorable for the utilization of SiC$_2$N.
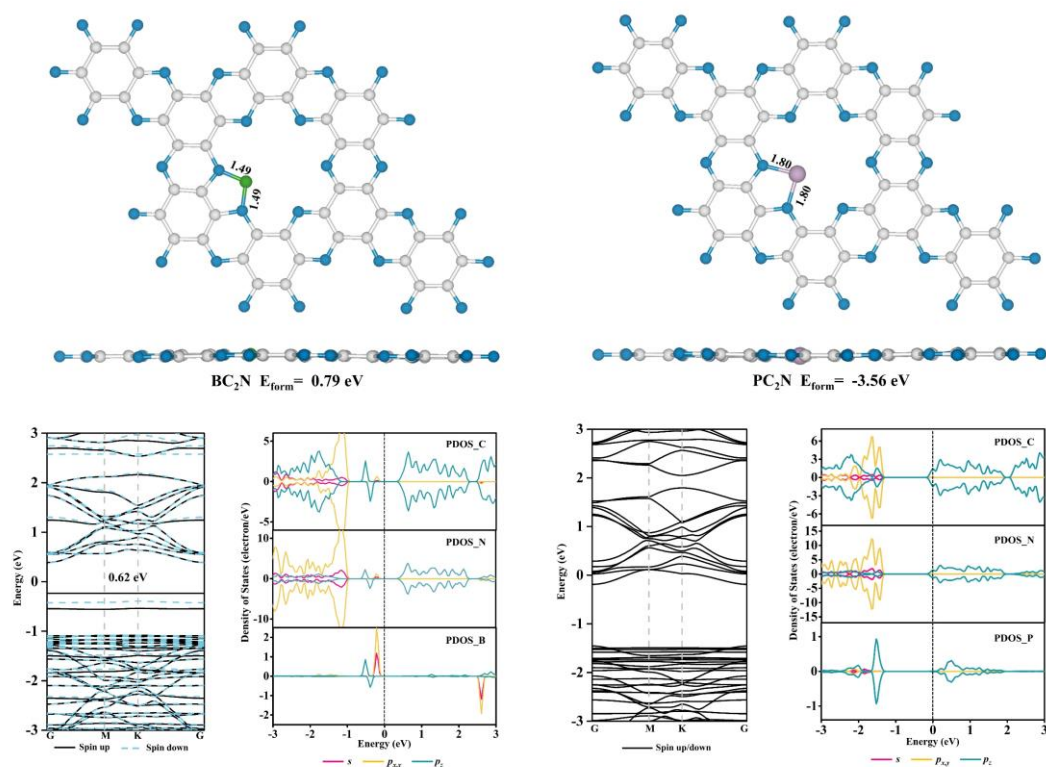
Figure S31. The optimal configuration, band structure, and partial density of states of BC$_2$N and PC$_2$N.
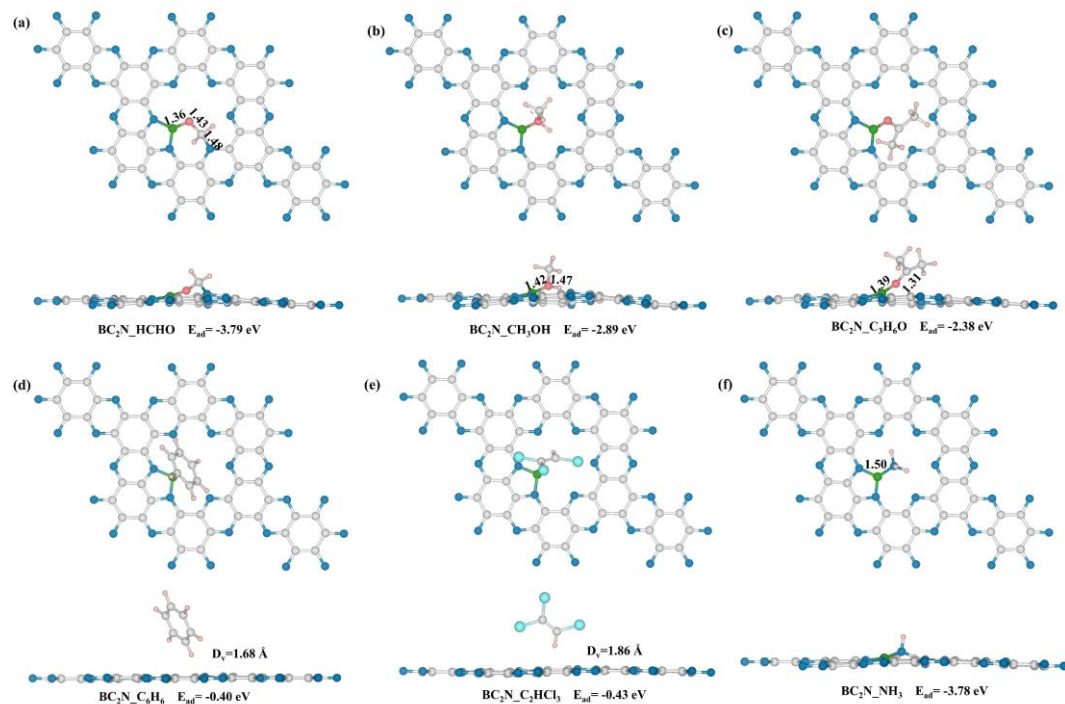
Figure S32. The optimal adsorption configurations of VOCs and ammonia on BC$_2$N. Bonds are in Å.
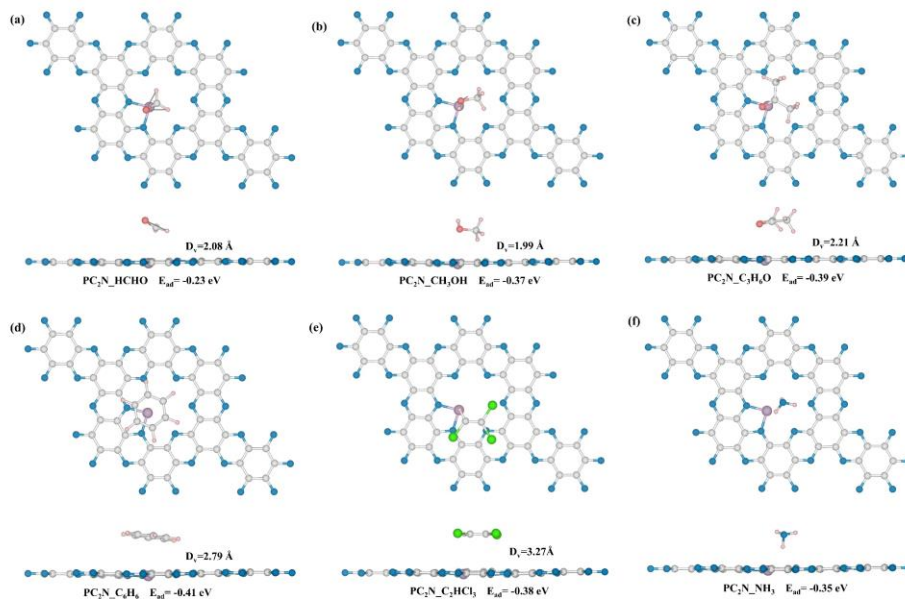
Figure S33. The optimal adsorption configurations of VOCs and ammonia on PC$_2$N. Bonds are in Å.
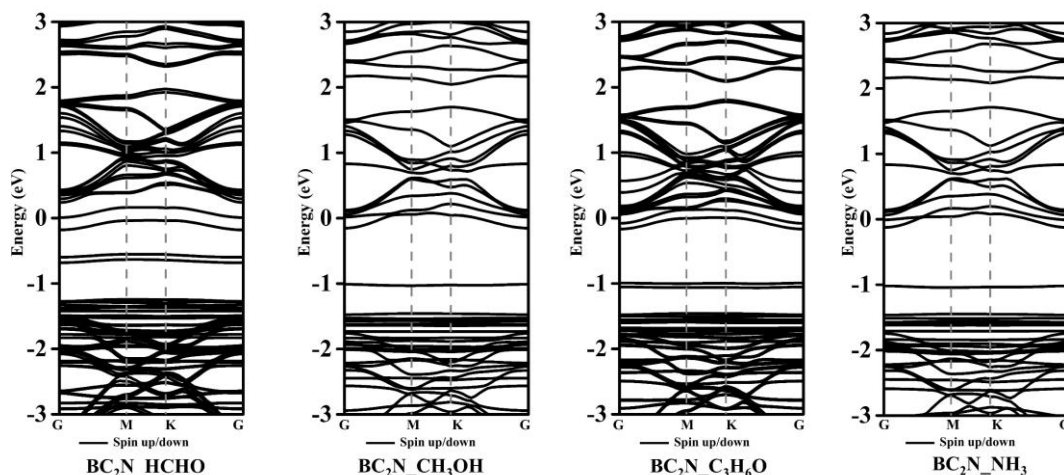
Figure S34. The band structure of BC$_2$N_HCHO, BC$_2$N_CH$_3$OH, BC$_2$N_C$_3$H$_6$O, and BC$_2$N_NH$_3$ systems.

In this section, we further investigated the sensor performance of nonmetal boron (B) and phosphorus (P) doped C$_2$N towards VOCs and ammonia. The B- and P- doped C$_2$N have been theoretically proposed by Ling et al.[3] and Wu et al.[4] for the NRR and NORR applications, respectively, and their optimal doping configurations were shown in Figure S31. The formation energies of B- or P- doped C$_2$N were calculated by the following equation:

$$E_{form}=E(XC_2N)-E(C_2N)-\mu(X) \ (X=B, P) \tag{2}$$

where the E(XC$_2$N) and E(C$_2$N) were the total electronic energies of BC$_2$N (or PC$_2$N) and pristine C$_2$N, respectively. The formation energies for BC$_2$N and PC$_2$N are 0.76 and -3.56 eV, respectively. Although the formation energy of BC$_2$N is positive, it is comparable to that of synthesized S-doped C$_2$N (0.85 eV), indicating high feasibility for the experimental synthesis of this B-doped C$_2$N layer. The electronic properties of BC$_2$N and PC$_2$N including band structure and partial density of states were shown in Figure S31 (c)-(f). One can see that both the BC$_2$N exhibit semiconductor feature with a band gap of 0.62 eV, and the PC$_2$N presents metallicity.

Regular calculations were carried out to search for the optimal adsorption configurations of VOCs and ammonia on BC$_2$N and PC$_2$N. And the optimal adsorption structures of BC$_2$N_gas and PC$_2$N_gas systems were screened out in Figure S32 and S33, respectively. Firstly, it can be seen that similar to SiC$_2$N, BC$_2$N exhibits outstanding selective adsorption performance for O-containing VOCs and ammonia, the adsorption energies of BC$_2$N towards HCHO, CH$_3$OH, C$_3$H$_6$O, and NH$_3$ are -3.79, -2.89, -2.38 and -3.78 eV, respectively. Whereas, the P-doped C$_2$N still presents weak affinity towards VOCs and NH$_3$, manifesting poor sensor performance. Then, the band structures of BC$_2$N_gas systems were further investigated in Figure S34. It can be seen that after the O-containing VOCs and NH$_3$ adsorption, the BC$_2$N_gas systems all present quite a small band gap (~0 V), indicating the enhancement of the conductivity. Nevertheless, the BC$_2$N_gas systems need a long recovery time or high operation temperature (see Table S3). Therefore, comparing B- and P-doped C$_2$N, the SiC$_2$N is more suitable as a sensor for VOCs and ammonia.
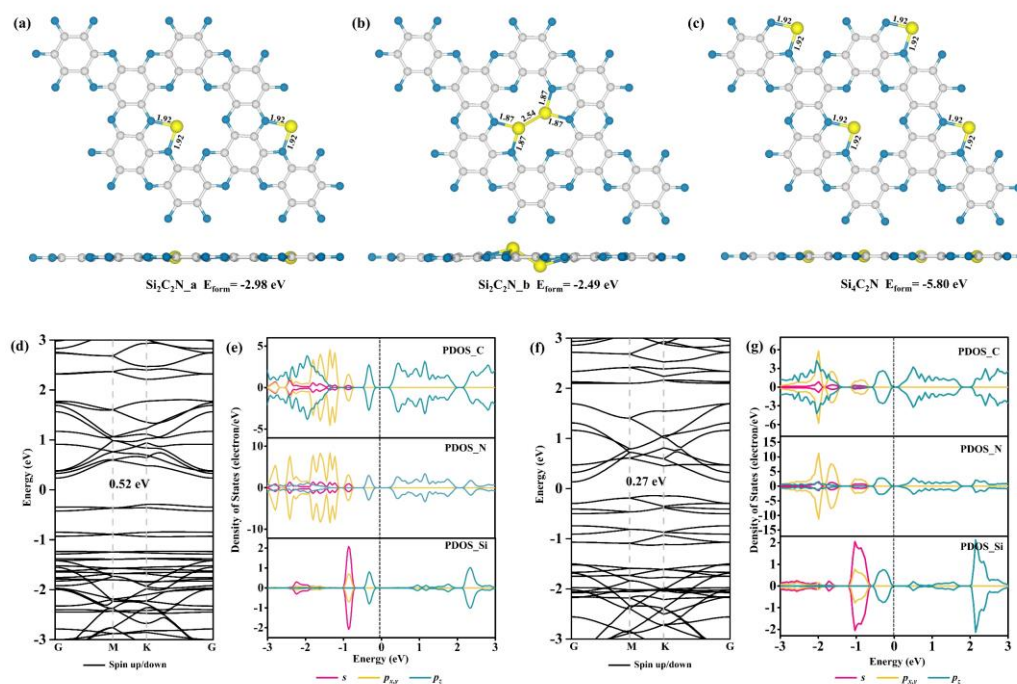
Figure S35. The optimized configurations of (a) Si$_2$C$_2$N_a, (b) Si$_2$C$_2$N_b, and (c) Si$_4$C$_2$N; the band structure of (d) Si$_2$C$_2$N and (f) Si$_4$C$_2$N; the partial density of states of (e) Si$_2$C$_2$N and (g) Si$_4$C$_2$N.
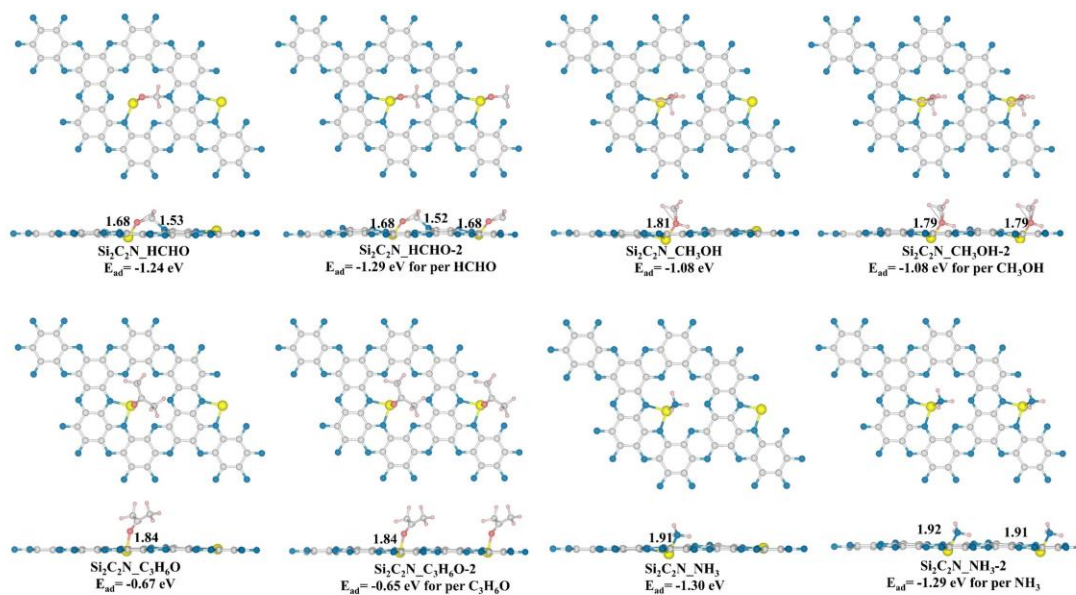
Figure S36. The optimized configurations of HCHO, CH_3OH, C_3H_6O, and NH_3 on Si_2C_2N. Bonds are in Å.
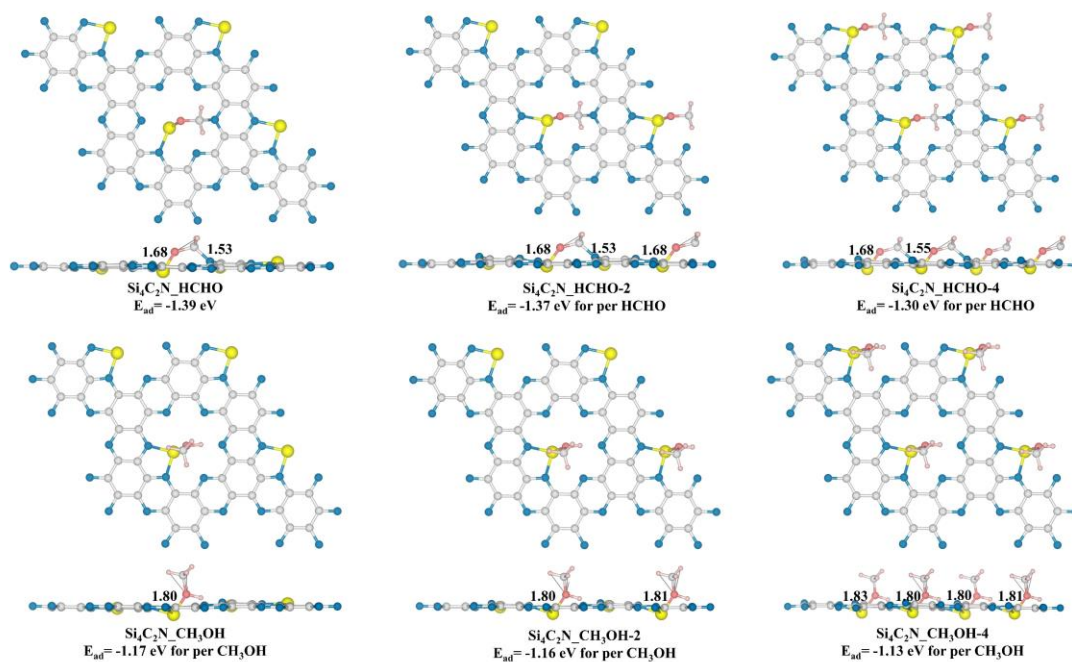
Figure S37. The optimized configurations of HCHO and CH_3OH on Si_4C_2N. Bonds are in Å.
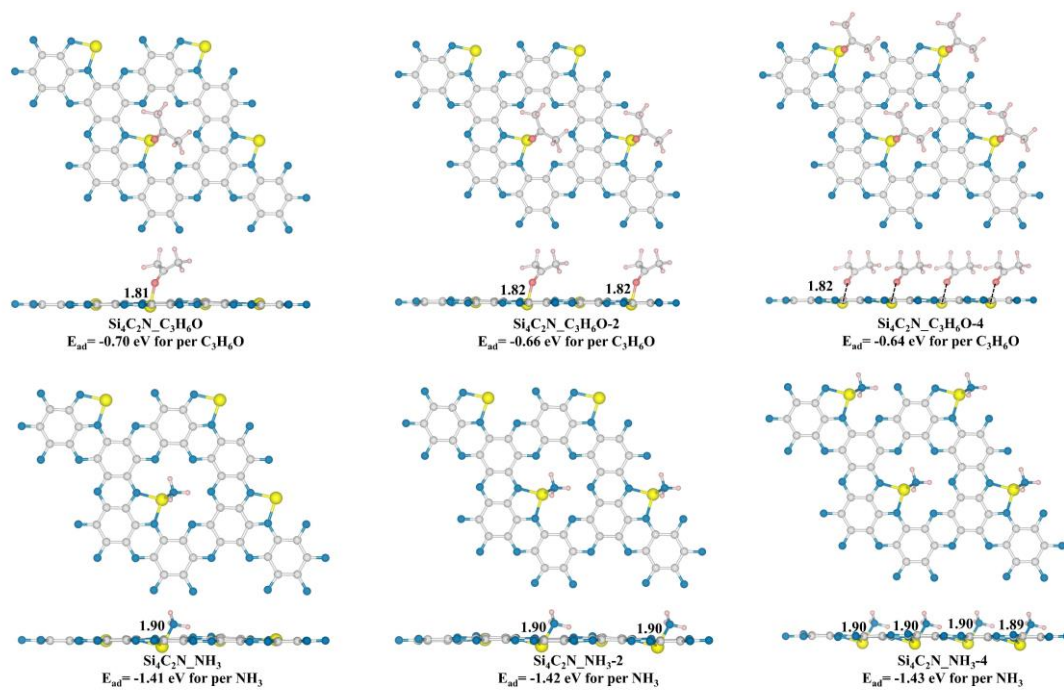
Figure S38. The optimized configurations of C_3H_6O, and NH_3 on Si_4C_2N. Bonds are in Å.

Table S1. The sensitivity of some other sensor materials reported in previous studies.

Sensors	Target gas	S (298 K)	τ (348 K)	τ (398 K)	ref
Pt-decorated P	Methanol	40%			[5]
Si-GreenP	acetone	~10^8			[6]
Pt-GreenP	C_2H_2	98.1%			[7]
	CH_4	39.3%			
	H_2	80.9%			
Ni-MoTe2	NO	99.8%			[8]
	NO_2	98.4%			
black phosphorus	CO_2	191%			[9]
vacancy-doped	CO_2	1254%			
black phosphorus					
Rh-BN	H_2S	9.36×10^{11}	1.78×10^{10}	9.20×10^8	[10]
	SO_2	4.79×10^7	3.30×10^6	5.01×10^5	
	SOF_2	1.63×10^5	2.91×10^4	8.00×10^3	
	SO_2F_2	9.10×10^4	1.76×10^4	5.17×10^3	
BC_3	gamma-hydroxybutyric acid	485			[11]
As-BN	SO_2F_2	4.38×10^{14}	3.45×10^{12}	9.17×10^{10}	[12]
	CO_2	3.35×10^{-1}	4.43×10^{-1}	3.78×10^{-1}	
	H_2O	2.88×10^{-1}	2.42×10^{-1}	2.09×10^{-1}	
Pd-BN	SO_2	41.04%			[13]
	SOF_2	108.14%			
	SO_2F_2	2.55%			

Table S2. The adsorption energies and recovery time of gases co-adsorption on SiC$_2$N sheet.

	E_{ad} (eV)	τ (300 K) (UV light)	τ (350 K) (UV light)	τ (400 K) (UV light)
SiC$_2$N_HCHO-2	-1.19	9.66×10^3	1.35×10^1	9.74×10^{-2}
SiC$_2$N_CH$_3$OH-2	-0.63	3.80×10^{-6}	1.17×10^{-7}	8.61×10^{-9}
SiC$_2$N_C$_3$H$_6$O-2	-0.65	8.24×10^{-6}	2.27×10^{-7}	1.54×10^{-8}
SiC$_2$N_NH$_3$-2	-1.29	4.62×10^5	3.71×10^2	1.77×10^0
SiC$_2$N_NH$_3$-HCHO	-1.27	2.13×10^5	1.91×10^2	9.92×10^{-1}
SiC$_2$N_NH$_3$-CH$_3$OH	-0.23	7.29×10^{-13}	2.05×10^{-13}	7.89×10^{-14}
SiC$_2$N_NH$_3$-C$_3$H$_6$O	-0.70	5.70×10^{-5}	1.19×10^{-6}	6.56×10^{-8}
SiC$_2$N_HCHO-CH$_3$OH	-0.25	1.58×10^{-12}	3.97×10^{-13}	1.41×10^{-13}
SiC$_2$N_HCHO-C$_3$H$_6$O	-0.67	1.79×10^{-5}	4.41×10^{-7}	2.75×10^{-8}
SiC$_2$N_CH$_3$OH-C$_3$H$_6$O	-0.70	5.70×10^{-5}	1.19×10^{-6}	6.56×10^{-8}

Table S3. The recovery time of BC$_2$N_gas systems under UV light

	τ (300 K) (UV light)	τ (700 K) (UV light)	τ (1100 K) (UV light)
BC$_2$N_HCHO	4.46×10^{47}	1.09×10^{11}	2.29×10^1
BC$_2$N_CH$_3$OH	1.11×10^{34}	2.81×10^5	4.46×10^{-3}
BC$_2$N_C$_3$H$_6$O	9.33×10^{23}	1.35×10^1	7.96×10^{-6}
BC$_2$N_NH$_3$	3.03×10^{47}	1.61×10^{11}	2.06×10^1

Table S4. The band gap and recovery time of $Si_nC_2N\_gas$ systems based on the PBE functional.

	Eg	τ (300 K) (UV light)	τ (350 K) (UV light)	τ (400 K) (UV light)
$Si_2C_2N\_HCHO\text{-}2$	0.03	4.62×10^5	1.13×10^2	1.77×10^0
$Si_2C_2N\_CH_3OH\text{-}2$	0	1.37×10^2	1.30×10^{-1}	4.01×10^{-3}
$Si_2C_2N\_C_3H_6O\text{-}2$	0.04	8.24×10^{-6}	1.25×10^{-7}	1.54×10^{-8}
$Si_2C_2N\_NH_3\text{-}2$	0	4.62×10^5	1.13×10^2	1.77×10^0
$Si_4C_2N\_HCHO\text{-}2$	0	1.02×10^7	1.49×10^3	1.80×10^1
$Si_4C_2N\_HCHO\text{-}4$	0	6.80×10^5	1.56×10^2	2.37×10^0
$Si_4C_2N\_CH_3OH\text{-}2$	0	3.03×10^3	1.71×10^0	4.08×10^{-2}
$Si_4C_2N\_CH_3OH\text{-}4$	0	9.49×10^2	6.52×10^{-1}	1.71×10^{-2}
$Si_4C_2N\_C_3H_6O\text{-}2$	0	1.21×10^{-5}	1.72×10^{-7}	2.06×10^{-8}
$Si_4C_2N\_C_3H_6O\text{-}4$	0	5.60×10^{-6}	9.05×10^{-8}	1.15×10^{-8}
$Si_4C_2N\_NH_3\text{-}2$	0	7.04×10^7	7.46×10^3	7.69×10^1
$Si_4C_2N\_NH_3\text{-}4$	0	1.04×10^8	1.03×10^4	1.03×10^2

References

1. Baikie, I.D.; Mackenzie, S.; Estrup, P.J.Z.; Meyer, J.A. Noise and the Kelvin method. *Rev. Sci. Instrum.* **1991**, *62*, 1326-1332. https://doi.org/10.1063/1.1142494.
2. Richardson, O.W. Electron Emission from Metals as a Function of Temperature. *Phy. Rev.* **1924**, *23*, 153-155. https://doi.org/10.1103/PhysRev.23.153.
3. Ji, S.; Wang, Z.; Zhao, J. A boron-interstitial doped C_2N layer as a metal-free electrocatalyst for N_2 fixation: a computational study. *J. Mater. Chem*. A **2019**, *7*, 2392-2399. https://doi.org/10.1039/C8TA10497B
4. Wu, Q.; Wang, H.; Shen, S.; Huang, B.; Dai, Y.; Ma, Y. Efficient nitric oxide reduction to ammonia on a metal-free electrocatalyst. *J. Mater. Chem. A* **2021**, *9*, 5434–5441. https://doi.org/10.1039/d0ta11209g.
5. Aasi, A.; Aghaei, S. M.; Panchapakesan, B. Pt-decorated phosphorene as a propitious room temperature VOC gas sensor for sensitive and selective detection of alcohols. *J. Mater. Chem.* C **2021**, 9, 9242-9250. https://doi.org/10.1039/D3TC00626C.
6. Singsen, S.; Watwiangkham, A.; Ngamwongwan, L.; Fongkaew, I.; Jungthawan, S.; Suthirakun, S. Defect Engineering of Green Phosphorene Nanosheets for Detecting Volatile Organic Compounds: A Computational Approach. *ACS Appl. Nano Mater.* **2023**, *6*, 1496-1506. https://doi.org/10.1021/acsanm.2c05567.
7. Aasi, A.; Javahersaz, R.; Aghaei, S. M.; Panchapakesan, B. Novel green phosphorene as a superior gas sensor for dissolved gas analysis in oil transformers: using DFT method. *Mol Simul* **2022,** *48*, 541-550. https://doi.org/10.1080/08927022.2022.2030863.
8. Cao, W.; Zhao, Q.; Yang, L.; Cui, H. Enhanced NO_x adsorption and sensing properties of MoTe2 monolayer by Ni-doping: A first-principles study. *Surf. Interfaces* **2021**, *26*, 101372. https://doi.org/10.1016/j.surfin.2021.101372.
9. Ghashghaee, M.; Ghambarian, M. Highly improved carbon dioxide sensitivity and selectivity of black phosphorene sensor by vacancy doping: A quantum chemical perspective. *Int J Quantum Chem* **2020**, *120*, e26265. https://doi.org/10.1002/qua.26265.
10. Xia, S.; Tao, L.; Jiang, T.; Sun H.; Li, J. Rh-doped h-BN monolayer as a high sensitivity SF_6 decomposed gases sensor: A DFT study. *Appl. Surf. Sci.* **2021**, *536*, 619-626. https://doi.org/10.1016/j.apsusc.2020.147965.
11. Wang, X.L. Potential application of BC_3 nanotubes as a gamma-hydroxybutyric acid drug sensor: A DFT study. *Comput Theor Chem* **2021**, *1202*, 113299. https://doi.org/ 10.1016/j.comptc.2021.113299.
12. Long, Y.; Xia, S.-Y.; Guo, L.-Y.; Tan, Y.; Huang, Z., As-Doped h-BN Monolayer: A High Sensitivity and Short Recovery Time SF_6 Decomposition Gas Sensor. *Sensors* **2022**, *22* 4797. https://doi.org/10.3390/s22134797.
13. Ma, S. X.; Li, D. J.; Rao, X. J.; Xia, X. F.; Su, Y.; Lu, Y. F., Pd-doped h-BN monolayer: a promising gas scavenger for SF_6 insulation devices. *Adsorption* 2020, 26, 619-626. https://doi.org/10.1007/s10450-020-00226-3.